

# The Hubble Deep Field South – STIS Imaging<sup>1</sup>.

Jonathan P. Gardner<sup>2</sup>, Stefi A. Baum<sup>3</sup>, Thomas M. Brown<sup>2,7</sup>, C. Marcella Carollo<sup>4,8,9</sup>, Jennifer Christensen<sup>3</sup>, Ilana Dashevsky<sup>3</sup>, Mark E. Dickinson<sup>3</sup>, Brian R. Espey<sup>3,10</sup>, Henry C. Ferguson<sup>3</sup>, Andrew S. Fruchter<sup>3</sup>, Anne M. Gonnella<sup>3</sup>, Rosa A. Gonzalez-Lopezlira<sup>3</sup>, Richard N. Hook<sup>5</sup>, Mary Elizabeth Kaiser<sup>2,4</sup>, Crystal L. Martin<sup>3,8</sup>, Kailash C. Sahu<sup>3</sup>, Sandra Savaglio<sup>3,10</sup>, T. Ed Smith<sup>3</sup>, Harry I. Teplitz<sup>2,7</sup>, Robert E. Williams<sup>3</sup>, Jennifer Wilson<sup>3,11</sup>

## ABSTRACT

We present the imaging observations made with the Space Telescope Imaging Spectrograph of the Hubble Deep Field – South. The field was imaged in 4 bandpasses: a clear CCD bandpass for 156 ksec, a long-pass filter for 22–25 ksec per pixel typical exposure, a near-UV bandpass for 23 ksec, and a far-UV bandpass for 52 ksec. The clear visible image is the deepest observation ever made in the UV-optical wavelength region, reaching a  $10\sigma$  AB magnitude of 29.4 for an object of area 0.2 square arcseconds. The field contains QSO J2233-606, the target of the STIS spectroscopy, and extends  $50'' \times 50''$  for the visible images, and  $25'' \times 25''$  for the ultraviolet images. We present the images, catalog of objects, and galaxy counts obtained in the field.

---

<sup>1</sup>Based on observations made with the NASA/ESA *Hubble Space Telescope*, obtained from the Space Telescope Science Institute, which is operated by the Association of Universities for Research in Astronomy, Inc., under NASA contract NAS 5-26555.

<sup>2</sup>Laboratory for Astronomy and Solar Physics, Code 681, Goddard Space Flight Center, Greenbelt MD 20771

<sup>3</sup>Space Telescope Science Institute, 3700 San Martin Drive, Baltimore MD 21218

<sup>4</sup>Dept. of Physics and Astronomy, Johns Hopkins University, Baltimore MD 21218

<sup>5</sup>Space Telescope-European Coordinating Facility, Karl Schwarzschild Strasse 2, D-85748, Garching bei München, Germany

<sup>6</sup>European Southern Observatory, Karl-Schwarzschild-Strasse 2, D-85748 Garching bei München, Germany

<sup>7</sup>NOAO Research Associate

<sup>8</sup>Hubble Fellow

<sup>9</sup>Currently at Columbia University, Department of Astronomy, Mail Code 5246 Pupin Hall, 550 West 120th Street, New York NY 10027

<sup>10</sup>On assignment from the Astrophysics Division, Space Science Department, European Space Agency

<sup>11</sup>Currently at The Observatories of the Carnegie Institution of Washington, 813 Santa Barbara, Pasadena, CA 91101

## 1. Introduction

The Space Telescope Imaging Spectrograph (STIS) (Kemble et al. 1997; Woodgate et al. 1998; Walborn & Baum 1998) was used during the Hubble Deep Field – South (HDF–S) (Williams et al. 1999) observations for ultraviolet spectroscopy (Ferguson et al. 1999) and ultraviolet and optical imaging. In this paper we present the imaging data.

The Hubble Deep Field – North (HDF–N) (Williams et al. 1996) is the best studied field on the sky, with  $>1$  Msec of Hubble Space Telescope (HST) observing time (including follow-up observations by Thompson et al. 1999 and Dickinson et al. 1999), and countless observations with ground-based telescopes (e.g., Cohen et al. 1996; Connolly et al. 1997). Results obtained to date include a measurement of the ultraviolet luminosity density of the universe at  $z > 2$  (Madau et al. 1996), the morphological distribution of faint galaxies (Abraham et al. 1996), galaxy-galaxy lensing (Hudson et al. 1998), and halo star counts (Elson, Santiago & Gilmore 1996). See Ferguson (1998) and Livio, Fall & Madau (1998) for reviews and further references. The HDF–S differs from the HDF–N in several ways. First, the installation of STIS and NICMOS on HST in 1997 February has enabled parallel observations with three cameras. In addition to the STIS data, the HDF–S dataset includes deep WFPC2 imaging (Casertano et al. 1999), deep near-infrared imaging (Fruchter et al. 1999), and wider-area flanking field observations (Lucas et al. 1999). Second, the STIS observations were centered on QSO J2233-606, at  $z \approx 2.24$ , to obtain spectroscopy. Finally, the field was chosen in the southern HST continuous viewing zone in order to enable follow-up observations with ground-based telescopes in the southern hemisphere.

In section 2 we describe the observations. In section 3 we describe the techniques we used to reduce the CCD images. In section 4 we describe the reduction of the MAMA images. In section 5 we describe the procedures used to catalog the images. In section 6 we present some statistics of the data, including galaxy number counts and color distributions. Our purpose in this paper is to produce a useful reference for detailed analysis of the STIS images. Thus for the most part we refrain from model comparisons and speculation on the significance of the results. We expect the STIS images to be useful for addressing a wide variety of astronomical topics, including the sizes of the faintest galaxies, the ultraviolet-optical color evolution of galaxies, the number of faint stars and white dwarfs in the galactic halo, and the relation between absorption line systems seen in the QSO spectrum and galaxies near to the line of sight. We also expect the observations to be useful for studying sources very close to the quasar, and perhaps for detecting the host galaxy of the quasar. However, this may require a re-reduction of the images, as the quasar is saturated in all of the CCD exposures, and there are significant problems with scattered light and reflections.

## 2. Description of the observations

The images presented here were taken in 4 different modes, 50CCD (Figure 1), F28X50LP (Figure 2), NUVQTZ (Figure 3), and FUVQTZ (Figure 4). The 50CCD and F28X50LP modes used the Charge Coupled Device (CCD) detector. The 50CCD is a clear, filterless mode, while the F28X50LP mode uses a long-pass filter beginning at about 5500Å. The FUVQTZ and NUVQTZ used the Multi-Anode Microchannel Array (MAMA) detectors as imagers with the quartz filter. The quartz filter was selected to reduce the sky noise due to airglow to levels below the dark noise. The effective areas of the 4 modes are plotted in Figure 5, along with a pseudo- $B_{430}$  bandpass constructed from the 50CCD and F28X50LP fluxes. The MAMA field of view is a square, 25" on a side, and was dithered so that the observations include data on a field approximately 30" square. The 50CCD mode is filterless imaging with a CCD. The field of view is a square 50" on a side, and the dithering extends to a square 60" on a side. The F28X50LP is a long-pass filter that vignettes the field of view of the CCD to a rectangle  $28 \times 50"$ . The observations were dithered to image the entire field of view of the 50CCD observations, although the exposure time per point on the sky is thus approximately half the total exposure time spent in this mode. The original pixel scale is  $0.0244" \text{ pix}^{-1}$  for the MAMA images, and  $0.05071" \text{ pix}^{-1}$  for the CCD images. The final combined images have a scale of  $0.025" \text{ pix}^{-1}$  in all cases. Table 1 describes the observations. The filterless 50CCD observations correspond roughly to V+I, and reach a depth of 29.4 AB magnitudes at  $10\sigma$  in a 0.2 square arcsecond aperture (320 drizzled pixels). This is the deepest exposure ever made in the UV-optical wavelength region.

### 2.1. Selection of the Field

Selection of the field is described by Williams et al. (1999). The QSO is at RA =  $22^{\text{h}}33^{\text{m}}37.5883^{\text{s}}$ , Dec =  $-60^{\circ}33'29.128"$  (J2000). The errors on this position are estimated to be less than 40 milli-arcseconds (Zacharias et al. 1998). The position of the QSO on the 50CCD and F28X50LP images is x=1206.61, y=1206.32, and on the MAMA images is x=806.61, y=806.32.

### 2.2. Test Data

Test observations of the field were made in 1997 October. These data are not used in the present analysis. While the test exposures do not add significantly to the exposure time, they would provide a one-year baseline for proper motion studies of the brighter objects.

### 2.3. Observing Plan

The STIS observations were scheduled so that the CCD was used in the orbits that were impacted by the South Atlantic Anomaly, and the MAMAs were used in the clear orbits. The observations were made in the continuous viewing zone, and therefore were all made close to the limb of the Earth. The G430M spectroscopy, all of which was read-noise limited, was done during the day or bright part of the orbit, while the CCD imaging was all done during the night or dark part of the orbit. The MAMA imaging, done with the quartz filter, is insensitive to scattered Earth light, and was therefore done during bright time. A more detailed discussion of the scheduling issues is given by Williams et al. (1999). The sky levels in the 50CCD images were approximately twice the square of the read noise, so these data are marginally sky noise limited. The MAMA images are limited by the dark noise.

### 2.4. Dithering and Rotation

The images were dithered in right ascension (RA) and declination (Dec) in order to sample the sky at the sub-pixel level. In addition, variations in rotation of about  $\pm 1$  degree were used to provide additional dithering for the WFPC2 and NICMOS fields during the STIS spectroscopic observations. The STIS imaging observations were interspersed with the STIS spectroscopic observations; therefore, all of the images were dithered in rotation as well as RA and Dec.

### 2.5. CR-SPLIT and pointing strategy

The CCD exposures were split into 2 or 3 CR-SPLITS that each have the same RA, Dec, and rotation. This facilitates cosmic ray removal, although as discussed below, this was only used in the first iteration of the data reduction. The final 50CCD image is the combination of 193 exposures making up 67 CR-SPLIT pointings. After standard pipeline processing, (including bias and dark subtraction, and flatfielding), each exposure is given a FLT file extension, and the cosmic-ray rejected combinations of each CR-SPLIT is given a CRJ file extension. The final F28X50LP image is the combination of 66 exposures making up 23 CR-SPLIT pointings. The F28X50LP image included 12 pointings at the northern part of the field, one pointing at the middle of the field, and 10 pointings at the southern half of the field.

## 2.6. PSF observations

In order to allow for PSF subtraction of the QSO present in the center of the STIS 50CCD image, two SAO stars of about 10 mag were observed in the filterless 50CCD mode before and after the main HDF-S campaign. The stars are SAO 255267, a G2 star, and SAO 255271, an F8 star, respectively. These targets have spectral energy distributions in the STIS CCD sensitivity range similar to that of the QSO. For each star, 32 different CR-SPLIT exposures were taken. The following strategy was used: (i) four different exposure times between 0.1 s and 5 s for each CR-SPLIT frame, to ensure high signal-to-noise in the wings while not saturating the center; (ii) a four-position dither pattern with quarter-pixel sampling and CR-SPLIT at each pointing with each exposure time; (iii) use of gain=4, to insure no saturation in the A-to-D conversion. During the observations for SAO255267, a failure in the guide star acquisition procedure caused the loss of its long-exposure (5 s) images. Gain=4 has a well-documented large scale pattern noise that must be removed, e.g., by Fourier filtering, before a reliable PSF can be produced. These data are not discussed further in this paper, but are available from the HST archive for further analysis.

## 3. Reduction of the CCD Images

### 3.1. Bias, Darks, Flats and Masks

Standard processing of CCD images involves bias and dark subtraction, flatfielding, and masking of detector defects. The bias calibration file used for the HDF-S was constructed from 285 individual exposures, combined together with cosmic-ray and hot-pixel trail rejection.

The dark file was constructed from a “superdark” frame and a “delta” dark frame. The superdark is the cosmic-ray rejected combination of over 100 individual 1200 s dark exposures taken over the several months preceding the HDF-S campaign. The delta dark adds into this high S/N dark frame the pixels that are more than  $5\sigma$  from the mean in the superdark-subtracted combination of 14 dark exposures taken during the HDF-S campaign. Calibration of the images with this dark frame removes most of the hot pixels but still leaves several hundred in each image.

An image mask was constructed to remove the remaining hot pixels and detector features. The individual cosmic-ray rejected HDF-S 50CCD exposures were averaged

together without registration. The remaining hot pixels were identified with the IRAF<sup>12</sup> COSMICRAYS task. These pixels were included in a mask that was used to reject pixels during the DRIZZLE phase. Pixels that were more than  $5\sigma$  below the mean sky background were also masked, as were the 30 worst hot pixel trails, and the unilluminated portions of the detector around the edges. Hot pixel trails run along columns and are caused by high dark current in a single pixel along the column.

Flatfielding was carried out by the IRAF/STSDAS CALSTIS pipeline using two reference files. The first, the PFLAT corrects for small-scale pixel-to-pixel sensitivity variations, but is smooth on large scales. This file was created from ground-test data but comparisons to a preliminary version of the on-orbit flat revealed only a few places where the difference was more than 1%. The CCD also shows a 5-10% decrease in sensitivity near the edges due to vignetting. This illumination pattern was corrected by a low-order fit to a sky flat constructed from the flanking field observations.

### 3.2. Shifts and rotations

After pipeline processing, the CCD images were reduced using the IRAF/STSDAS package DITHER, and test versions called XDITHER, and XDITHERII. These packages include the DRIZZLE software (Fruchter & Hook 1998; Fruchter et al. 1998; Fruchter 1998). We used DRIZZLE version 1.2, dated 1998 February. The test versions differ from the previously released version primarily in their ability to remove cosmic rays from each individual exposure, and include tasks that have not yet been released.

The XDITHERII package uses an iterative process to reject cosmic rays and determine the x and y sub-pixel shifts, which we summarize here. The standard pipeline rejects cosmic rays using each CR-SPLIT of 2 or 3 images. The resulting CRJ files are used as the first iteration, we determine the x and y shifts, and the files are median combined. The resulting preliminary combination is then shifted back into the frame of each of the original exposures (FLT files), and a new cosmic ray mask is made. By comparing each exposure to a high signal-to-noise combination of all of the data, we are less likely to leave cosmic ray residuals. The x and y shifts are determined at each iteration as well.

The rotations used in combining the data were determined from the ROLL\_AVG

---

<sup>12</sup>IRAF is distributed by the National Optical Astronomy Observatories, which are operated by the Association of Universities for Research in Astronomy, Inc., under cooperative agreement with the National Science Foundation.

parameter in the jitter files, using the program BEARING. We did not seek to improve on these rotations via cross-correlation or any other method. We did use cross-correlation to determine the x and y shifts.

Determination of the sub-pixel x and y shifts was done with an iterative procedure. The first iteration was obtained by determining the centroid of the bright point source just west of the QSO, using the pipeline cosmic-ray rejected CRJ files. We could not use cross-correlation in this first iteration, because the very bright star on the southern edge of the field was present on images taken at some, but not all, dither positions, which corrupted the cross-correlation. The source we used for centroiding was clearly visible on all of the 50CCD and F28X50LP frames.

Using these shifts (which were accurate to better than 1 pixel), we created a preliminary combined image. After pipeline processing and cosmic ray rejection, the DRIZZLE program was used to shift and rotate each sc crj file onto individual outputs, without combining them. We then used the task IMCOMBINE to create a median combination of the files. This preliminary image was then shifted and rotated back into the frame of each individual exposure using the XDITHER task, BLOT, ready for the next iteration of the cosmic-ray rejection procedure.

### 3.3. Cosmic ray rejection

In this iteration, we discarded the CRJ files, and went back to the FLT files, in which each exposure had undergone bias and dark subtraction and flatfielding, but not cosmic-ray rejection. Each exposure was compared to the blotted image, and a cosmic-ray mask for that exposure was created from all of the pixels that differed (positively or negatively) by more than a given threshold from the blotted image. In the version 1.0 released 50CCD image, this threshold was set to be  $5\sigma$ . However, we believe that a small error in the sky level determination, introduced by the amplifier ringing correction discussed below, meant that our rejection was approximately at the  $3\sigma$  level. The cosmic ray masks were multiplied by the hot pixel masks discussed above, and resulted in about 8% of the pixels being masked as either cosmic rays or hot pixels. This is, perhaps, overly conservative. A less conservative cut (after correcting the error in the sky value) would result in slightly higher exposure time per pixel, and thus an improvement of 1-2% in the signal to noise ratio. The cosmic ray mask was combined with the hot pixel and cosmetic defect mask.

This problem with the sky value was corrected in the F28X50LP image, and a  $3\sigma$  level was used in the cosmic ray rejection.

### 3.4. Amplifier ringing correction

Horizontal features due to amplifier ringing, varying in pattern from image to image, were present in most of the STIS CCD frames. When a pixel saw a highly saturated signal, the bias level was depressed in the readout for the next few rows. The very high signals causing this ringing came from hot pixels and from the saturated QSO. The signal-to-noise ratio in the overscan region of the detector was not sufficient to remove these features well. We removed them with a procedure that subtracted on a row-by-row basis, from each individual image, the weighted average of the background as derived from the innermost 800 columns after masking and rejecting “contaminated” pixels. The masks included all visible sources, hot pixels, and cosmic-ray hits. The source mask was determined from the initial registered median-combined image, shifted back to the reference frame of each of the individual images. For the unmasked pixels in each row, the 50 highest and lowest were rejected and the mean of the remaining pixels was subtracted from the each pixel in that row.

Heavily smoothing the images reveals very slight horizontal residuals that were not removed by the present choice of parameters in this process.

### 3.5. Drizzling it all together

The final image combination was done by drizzling the amplifier-ringing corrected pipeline products together onto a single output image. The exposures were weighted by the square of the exposure time, divided by the variance, which is  $(\text{sky} + \text{rn}^2 + \text{dark})$ . The rotations were corrected so that North is in the  $+y$  direction, and the scale used was 0.492999 original CCD pixels per output pixel so that the final pixel scale is exactly 0.025 arcsec/pixel. For the 50CCD data we used a `PIXFRAC=0.1`, which is approximately equivalent to interleaving, where each input pixel falls on a single output pixel. For the F28X50LP data we used `PIXFRAC=0.6`, as a smaller `PIXFRAC` left visible holes in the final image. See Fruchter & Hook (1998) for a discussion of the meaning of the `DRIZZLE` parameters. The point spread functions of bright, non-saturated point sources are shown in Figure 6. The sources selected are the point source just to the west of the quasar in the 50CCD and F28X50LP images, and the QSO in the MAMA images.

The final image is given in counts per second, which can be converted to magnitudes on the STMAG system using the photometric zeropoints given by the `PHOTFLAM` parameter supplied in the image headers. We used the pipeline photometric zeropoints for the 50CCD and MAMA images, but revised the F28X50LP zeropoint by 0.1 magnitude based on

a comparison of STIS photometry of the HST calibration field in  $\omega$  Centauri with the ground-based photometry of Walker (1994). The zeropoints in the AB magnitude system which we used are 26.386, 25.291, 23.887, and 21.539, for the 50CCD, F28X50LP, NUVQTZ and FUVQTZ respectively. We also supply the weight image, which is the sum of the weights falling on each pixel. For the F28X50LP image, we supply an exposure-time image, which is the total exposure time contributing to each pixel. We have multiplied this image by the area of the output pixels. The world coordinate system in the headers was corrected so that North is exactly in the +y direction, and the pixel scale is exactly 0.025 arcsec/pixel.

### 3.6. Window reflection

A window in the STIS CCD reflects slightly out-of-focus light from bright sources to the  $+x$ ,  $-y$  direction (SW on the HDF-S images). The QSO is saturated in every 50CCD and F28X50LP exposure. The window reflection of the QSO is clearly visible in the F28X50LP image, but has been partially removed from the 50CCD image by the cosmic-ray rejection procedure. We wish to emphasize that it has only been partially removed, and there are remaining residuals. These residuals should not be mistaken for galaxies near the QSO, nor should they be mistaken for the host galaxy of the QSO. There is additional reflected light from the QSO (and from the bright star at the southern edge) evident in the images. We believe that the version 1.0 released images are not appropriate for searching for objects very close to or underlying the QSO, and that such a search would require re-processing the raw data with particular attention paid to the window reflection, other reflected light, and to the PSF of the QSO. The diffraction spikes of the QSO are smeared in the final images by the rotation of the individual exposures.

## 4. Reduction of the MAMA Images

The near-UV and far-UV images are respectively the weighted averages of 12 and 25 registered frames, with total exposure times of 22616 s and 52124 s. The MAMAs do not suffer from read noise or cosmic rays, and the quasar is not saturated in any of the UV data. However, the MAMAs do have calibration issues that must be addressed.

#### 4.1. Flats, Dark Counts, and Geometric Correction

Prior to combination, all frames were processed with CALSTIS, including updated high-resolution pixel-to-pixel flat field files for both UV detectors. Geometric correction and rescaling were applied in the final combinations via the DRIZZLE program. The quartz filter changes the far-UV plate scale relative to that in the far-UV clear mode, and so the relative scale between MAMA imaging modes was determined from calibration images of the globular cluster NGC 6681.

Dark subtraction for the near-UV image was done by subtracting a scaled and flat-fielded dark image from each near-UV frame. The scale for the dark image was determined by inspection of the right-hand corners of the near-UV image, because these portions of the detector are occulted by the aperture mask and thus only register dark counts. For the far-UV images, CALSTIS removes a nearly flat dark frame, but the upper left-hand quadrant of STIS far-UV frames contains a residual glow in the dark current after nominal calibration. This glow varies from frame to frame and also appears to change shape slightly with time. To remove the residual dark current, the 16 far-UV frames with the highest count rates in the glow region were co-added without object registration but with individual object masks for the only two obvious objects in the far-UV frames (the quasar and bright spiral NNE of the quasar). We then fit the result with a cubic spline to produce a glow profile. This profile was then scaled to the residual glow in each processed frame and subtracted prior to the final drizzle. Even during observations with a strong dark glow, where the dark count rate is an order of magnitude higher than normal, it is still very low, reaching rates no higher than  $6 \times 10^{-5}$  cts sec $^{-1}$  pix $^{-1}$ . The glow thus appears as a higher concentration of ones in a sea of zeros, and the subtraction of a smooth glow profile from such quantized data over-subtracts from the zeros and under-subtracts from the ones. These effects are visible in the corrected data, even when smoothed out considerably in the final drizzled far-UV image. A low-resolution flat-field correction was applied to the far-UV frames after subtraction of the residual dark glow. The near-UV frames require no low-resolution flat field correction.

#### 4.2. Shifts and Rotations

Currently, geometrically corrected NUVQTZ and FUVQTZ frames do not have the same plate scale. Although geometric correction, rotation, and rescaling is applied during the final summation of individual calibrated frames, we first produced a set of calibrated frames that included these corrections, in order to accurately determine the relative shifts between them; this information was then used in conjunction with these corrections in

the final drizzle. All near-UV and far-UV frames were geometrically corrected, rescaled to  $0.025''\ pix^{-1}$ , and rotated to align North with the +y image axis. The roll angle specified in the jitter files was used to determine the relative roll between frames, and the mean difference between the planned roll and the jitter roll determined the absolute rotation. It is difficult to determine accurate roll angles from the images themselves, because of the scarcity of objects in the MAMA images. All near-UV and far-UV frames were then cross-correlated against one of the far-UV frames to provide shifts in the output coordinate system. Note that centroiding on the quasar in all far-UV and near-UV frames yields the same shifts as cross-correlation, within 0.1 pixel.

### 4.3. Drizzling

The calibrated frames were drizzled to a  $1600 \times 1600$  pixel image, including the above corrections, rescaling, rotations, and shifts. We updated the world coordinate system in the image headers to exactly reflect the plate scale, alignment, and the astrometry of the quasar.

For both the far-UV and near-UV frames, individual pixels in each frame were weighted by the ratio of the exposure time squared to the dark count variance; this weights the exposures by  $(S/N)^2$  for sources that are fainter than the background. Although the variations in the far-UV dark profile are smooth, the near-UV dark profile is an actual sum of dark frames, and so we smoothed the near-UV dark profile to determine the weights. With this weighting algorithm, pixels in the upper left-hand quadrant of a given far-UV image contribute less when the dark glow is high, and contribute more when it is low. The statistical errors ( $\text{cts s}^{-1}$ ) in the final drizzled image, for objects below the background (e.g., objects other than the quasar), are given by the square root of the final drizzled weights file.

The drizzle “dropsize” (PIXFRAC) was 0.6, thus improving the resolution over a PIXFRAC of 1.0 (which would be equivalent to simple shift-and-add). The  $1600 \times 1600$  pixel format contains all dither positions, and pixels outside of the dither pattern are at a count rate of zero. The pixel mask for each near-UV input frame included the occulted corners of the detector, a small number of hot pixels, and pixels with relatively low response (those with values  $\leq 0.75$  in the high-resolution flat field). The pixel mask for each far-UV frame included hot pixels and all pixels flagged in the data quality file for that frame. When every input pixel drizzled onto a given output pixel was masked, that pixel was set to zero.

#### 4.4. Window Reflection

As with the CCD, a window reflection of the QSO appears in the near-UV image. This reflection appears  $\approx 0.2''$  east of the QSO itself, and should not be considered an astronomical object.

### 5. Cataloging

#### 5.1. Cataloging the Optical Images

The catalog was created using the SExtractor package (Bertin & Arnouts 1996), revision of 1998 November 19, with some minor modifications that were done for this application. We used two separate runs of SExtractor, and manually merged the resulting output catalogs. The first run used a set of parameters selected to optimize the detection of faint sources while not splitting what appeared to the eye to be substructure in a single object. We varied the parameters DETECT\_THRESH, DEBLEND\_MINCONT, BACK\_SIZE, and BACK\_FILTERSIZE. We decided to use a detection threshold corresponding to an isophote of  $0.65\sigma$ . Sources were required a minimum area of 16 connected pixels above this threshold. Deblending was done when the flux in the fainter object was a minimum of 0.03 times the flux in the brighter object. The background map was constructed on a grid of 60 pixels, and subsequently filtered with a  $3 \times 3$  median filter. Prior to cataloging, the image was convolved with a Gaussian kernel with full width half maximum of 3.4 pixels. As discussed in Fruchter & Hook (1998), the effects of drizzling on the photometry is no more than 2%, and in our well-sampled 50CCD field, the effects should be much less than this. This effect is smaller than other uncertainties in the photometry of extended objects.

The second run of SExtractor was optimized to detect objects that lay near the QSO and the bright star at the southern edge of the image. These objects tend to be blended in with the point source at the lower detection threshold. Although our catalog might include galaxies that are associated with absorption lines in the quasar spectrum, we did not attempt to subtract the quasar light from the image, and so the catalog does not include objects within  $3''$  of the quasar. The parameters used for the second run were the same as for the first run, with the exception of the DETECT\_THRESH parameter, which was set to  $3.25\sigma$ . This parameter not only sets the minimum flux level for detection, but also is the isophote used to determine the extent of the object. Several objects fall between the  $0.65\sigma$  isophote and the  $3.25\sigma$  isophote of the quasar. These are not deblended on the first SExtractor run, because their fluxes are below 0.03 of the quasar flux, but are detected (without the need for deblending) on the second run. Objects near the quasar

detected in the second run were added to the catalog generated by the first run, and flagged accordingly. Objects from the second run that were not confused with the quasar or the bright star were not included. The isophotal photometry of objects from the second run will not be consistent with the photometry of objects from the first run, because a different isophote was used. Eight objects were added to the catalog in this way.

In addition, 26 objects from the first SExtractor run were clearly spurious due to the diffraction spikes of the QSO and the bright star. These were manually deleted from the catalog.

Photometry of the F28X50LP image was done with SExtractor run in two-image mode, in which the objects were detected and identified on the 50CCD image, but the photometry was done in the other band. Isophotes and elliptical apertures are thus determined by the extent of the objects on the 50CCD images. Objects detected in the F28X50LP image but not on the 50CCD image are impossible, since it has a lower throughput and shorter exposure time.

## 5.2. Cataloging the Ultraviolet Images

Fluxes in the UV were calculated outside of SExtractor because it had some problems handling quantized low-signal data. To determine the gross flux, we summed the countrate within the area for each object appearing in the SExtractor 50CCD segmentation map. We then created an object mask by “growing” each object in the segmentation map, using the IDL routine DILATE, until it subtended an area three times its original size. The resulting mask excludes faint emission outside of the SExtractor isophotes for all known objects in the field. The sky was calculated from those exposed pixels within a  $151 \times 151$  pixel box centered on each object, excluding pixels from the mask. The mean countrate per pixel in this sky region was used to determine the background for each object (the median is not a useful quantity when dealing with very low quantized signals), and thus the net flux. Statistical errors per pixel for objects at or below the background are determined from the DRIZZLE weight image raised to the  $-1/2$  power. The statistical errors for the gross flux and sky flux were calculated using this pixel map of statistical errors, and thus underestimate the errors for bright objects such as the quasar.

Some objects that are fully-exposed in the CCD image do not fall entirely within the exposed area of the MAMA images; for these objects, we calculated the UV flux in the exposed area only, without correcting for the incomplete exposure, and flagged such objects accordingly. Objects were also flagged if the sky-box described above did not contain at

least 100 pixels (e.g., the quasar). For these objects, we calculated a global sky value from a larger  $685 \times 670$  pixel box, roughly centered in each MAMA image, that only includes areas fully exposed in the dither pattern, and excludes pixels in the object mask. When the net flux incorporates this global sky value, they have been flagged accordingly. We do not expect or see any evidence for objects in the ultraviolet images that do not appear on the 50CCD image.

### 5.3. The Catalog

The catalog is presented in Table 2, which contains a subset of the photometry. The full catalogs are available on the World Wide Web. For each object we report the following parameters:

**ID:** The SExtractor identification number. The objects in the list have been sorted by right ascension (first) and declination (second), and thus are no longer in catalog order. In addition, the numbers are no longer continuous, as some of the object identifications from the first SExtractor run have been removed. Objects from the second SExtractor run have had 10000 added to their identification numbers. These identification numbers provide a cross-reference to the segmentation maps.

**HDFS\_J22r-60d:** The minutes and seconds of right ascension and declination, from which can be constructed the catalog name of each object. To these must be added 22 hours (RA) and  $-60$  degrees (Dec). The first object in the catalog is HDFS\_J223333.69–603346.0, at RA  $22^h\ 33^m\ 33.69^s$ , Dec  $60\text{deg}\ 33'\ 46.0''$ , epoch J2000.

**x, y:** The x and y pixel positions of the object on the 50CCD and F28X50LP images. To get the x and y pixel positions on the MAMA images, subtract 400 from each.

$m_i, m_a$ : The isophotal ( $m_i$ ) and “mag\\_auto” ( $m_a$ ) 50CCD magnitudes. The magnitudes are given in the AB system (Oke 1971), where  $m = -2.5\log f_\nu - 48.60$ . The isophotal magnitude is determined from the sum of the counts within the detection isophote, set to be  $0.65\sigma$ . The “mag\\_auto” is an elliptical Kron (1980) magnitude, determined from the sum of the counts in an elliptical aperture. The semi-major axis of this aperture is defined by 2.5 times the first moments of the flux distribution within an ellipse roughly twice the isophotal radius. However if the aperture defined this way would have a semi-major axis smaller than than 3.5 pixels, a 3.5 pixel value is used.

**clr-lp:** Isophotal color, 50CCD–F28X50LP, in the AB magnitude system, as determined in the 50CCD isophote. SExtractor was run in two-image mode to determine

the photometry in the F28X50LP image, using the 50CCD image as the detection image. When the measured F28X50LP flux is less than  $2\sigma$ , we determine an upper limit to the color using the flux plus  $2\sigma$  when the measured flux is positive, and  $2\sigma$  when the measured flux is negative. We did not clip the 50CCD photometry.

**nuv-clr, fuv-clr:** Isophotal colors, NUVQTZ-50CCD and FUVQTZ-50CCD, in the AB magnitude system. Photometry in the MAMA images are discussed above. Photometry of objects falling partially outside the MAMA image are flagged and should not be considered reliable. When the measured flux is less than  $2\sigma$ , we give lower limits to the color as discussed above.

$r_h$ : The half-light radius of the object in the 50CCD image, given in milli-arcseconds. The half-light radius was determined by SExtractor to be the radius at which a circular aperture contains half of the flux in the “mag\_auto” elliptical aperture.

**s/g:** A star-galaxy classification parameter determined by a neural network within SExtractor, and based upon the morphology of the object in the 50CCD images (see Bertin & Arnouts 1996 for a detailed description of the neural network). Classifications near 1.0 are more like a point source, while classifications near 0.0 are more extended.

**flags:** Flags are explained in the table notes, and include both the flags returned by SExtractor, and additional flags we added while constructing the catalog.

## 6. Statistics

In this section we present several statistics of the data compiled from the catalog.

### 6.1. Source Counts

The source counts in the 50CCD image are given in Table 3, and plotted as a function of AB magnitude in Figure 7, where they are compared with the galaxy counts from the HDF-N WFPC2 observations, as compiled by Williams et al. (1996). The counts are compiled directly from the catalog, although all flagged regions have been excluded, so that the counts do not include objects near the edge of the image, or near the quasar. We plot only the Poissonian errors, although there might be an additional component due to large-scale structure. We plot all sources, including both galaxies and stars, although we do not expect stars to contribute substantially to the source counts. No corrections for detection completeness have been made, and the counts continue to rise until fainter than

30 mag. The turnover fainter than this is due to incompleteness; the counts do not turn over for astrophysical or cosmological reasons.

## 6.2. Colors and Dropouts

The 50CCD-F28X50LP colors of objects in the STIS images are plotted as points in Figure 8. Flagged objects have been removed from the sample. For comparison, we plot K-corrected (no-evolution) colors of the template galaxies in the Kinney et al. (1996) sample as a function of redshift on the left of the figure. The LP filter is able to distinguish blue galaxies at  $z < 2.5$ , but becomes dominated by the noise for blue galaxies fainter than 28 mag, and loses color resolution at  $z > 3$ , where the Ly $\alpha$  forest dominates the color in these bandpasses.

Because the F28X50LP bandpass is entirely contained within the 50CCD bandpass, it is possible, by subtracting an appropriately scaled version of the measured F28X50LP flux from the 50CCD flux, to construct a pseudo- $B_{430}$  measurement (see Figure 5). This pseudo- $B_{430}$  is combined with the NUVQTZ and the F28X50LP measurements in a color-color diagram in Figure 9. NUV drop-outs, indicated on this figure by the dashed line, are those objects with blue colors in the visible, but red colors in the UV, indicative of galaxies at  $z > \sim 1.5$ . These galaxies show blue colors characteristic of rapid star formation, while the red NUV to optical color is due to the Lyman break and absorption by the Ly $\alpha$  forest. The selection criteria were determined using the models of Madau et al. (1996). In an inset to Figure 9, we plot the efficiency of these criteria for selecting galaxies of high redshift. The solid line is the fraction of all of the models that meet these criteria, while the dotted line is the fraction of those models with ages  $< 10^8$  years and foreground-screen extinction less than  $A_B = 2$ . These criteria are very efficient at finding young, star-forming galaxies at  $1.5 < z < 3.5$ . We have removed point sources from this figure, including the bright object just west of the QSO, which is extremely red and is likely to be an M star.

In Figure 10 we give a FUV-NUV vs NUV-50CCD color-color plot showing FUV dropouts, where the Lyman break is passing through the FUV bandpass at  $z > 0.6$ . Of the 17 galaxies in the MAMA field with NUV magnitudes brighter than 28.4, only 3 have a clear signature of a Lyman break at  $0.6 < z < 1.5$ . However, the upper limits are sufficiently weak that roughly half the sample could be at  $z > 0.6$ .

## 7. Conclusions

We have presented the STIS imaging observations that were done as part of the Hubble Deep Field – South campaign. The 50CCD image is the deepest image ever made in the UV-optical wavelength region, and achieves a point source resolution near the diffraction limit of the HST. We have presented the catalog, and some statistics of the data. These data will be useful for the study of the number and sizes of faint galaxies, the UV-optical color evolution of galaxies, the number of faint stars and white dwarfs in the galactic halo, and the relation between absorption line systems seen in the QSO spectrum and galaxies near to the line of sight. Follow-up observations of the HDF-South fields by southern hemisphere ground-based telescopes, by HST, and by other space missions will also greatly increase our understanding of the processes of galaxy formation and evolution.

The images and catalog presented here are available on the World Wide Web at:  
[<http://www.stsci.edu/ftp/science/hdfsouth/hdfs.html>](http://www.stsci.edu/ftp/science/hdfsouth/hdfs.html).

We would like to thank all of the people who contributed to making the HDF-South campaign a success, including those who helped to identify a target quasar in the southern CVZ, and those who helped in planning and scheduling the observations. JPG, TMB, and HIT wish to acknowledge funding by the Space Telescope Imaging Spectrograph Investigation Definition Team through the National Optical Astronomical Observatories, and by the Goddard Space Flight Center. CLM and CMC wish to acknowledge support by NASA through Hubble Fellowship grants awarded by STScI.

## REFERENCES

- Abraham, R. G., Tanvir, N. R., Santiago, B. X., Ellis, R. S., Glazebrook, K., & van den Bergh, S. 1996, MNRAS, 279, L47
- Bertin, E., & Arnouts, S. 1996, A&AS, 117, 393
- Casertano, S., et al. 1999, in preparation
- Cohen, J. G., Cowie, L. L., Hogg, D. W., Songaila, A., Blandford, R., Hu, E. M., Shopbell, P. 1996, ApJ, 471, L5
- Connolly, A. J., Szalay, A. S., Dickinson, M., SubbaRao, M. U., & Brunner, R. J. 1997, ApJ, 486, L11
- Dickinson et al. 1999, ApJ, in press, astro-ph/9908083

- Elson, R. A. W., Santiago, B. X., & Gilmore, G. F. 1996, New Astronomy, 1, 1
- Ferguson, H. C., 1998, Reviews in Modern Astronomy, 11, 83
- Ferguson, H. C., et al. 1999, in preparation
- Fruchter, A. S., & Hook, R. N. 1998, astro-ph/9808087
- Fruchter, A. S. et al. 1998, in 1997 HST Calibration Workshop, ed. S. Casertano et al. (STScI)
- Fruchter, A. S. 1998, <http://www.stsci.edu/~fruchter/dither/dither.html>
- Fruchter, A. S. et al. 1999, in preparation
- Hudson, M. J., Gwyn, S. D. J., Dahle, H., & Kaiser, N. 1998, ApJ, 503, 531
- Kimble, R. A., et al. 1997, ApJ, 492, L83
- Kinney, A. L., Calzetti, D., Bohlin, R. C., McQuade, K., Storchi-Bergmann, T., & Schmitt, H. R. 1996, ApJ, 467, 38
- Kron, R. G. 1980, ApJS, 43, 305
- Livio, M., Fall, S. M., & Madau, P. (eds.) 1998, The Hubble Deep Field : proceedings of the Space Telescope Science Institute Symposium 11, (New York : Cambridge University Press)
- Lucas, R. A., et al. 1999, in preparation
- Madau, P., Ferguson, H. C., Dickinson, M. E., Giavalisco, M., Steidel, C. C. & Fruchter, A. 1996, MNRAS, 283, 1388
- Oke, J. B. 1971, ApJ, 170, 193
- Thompson, R. I., Storrie-Lombardi, L. J., Weymann, R. J., Rieke, M. J., Schneider, G., Stobie, E., & Lytle, D. 1999, 117, 17
- Walborn, N., & Baum, S. 1998, STIS Instrument Handbook, version 2.0, (Baltimore: STScI), <http://www.stsci.edu/instruments/stis>.
- Walker, A. R. 1994, PASP, 104, 828
- Williams, R. E., et al. 1996, AJ, 112, 1335
- Williams, R. E., et al. 1999, in preparation
- Woodgate, B. E., et al. 1998, PASP, 110, 1183
- Zacharias, N., et al. 1998, BAAS, 193, 75.09

NOTE: The resolution of this image has been reduced. Full resolution images are available at: <http://hires.gsfc.nasa.gov/~gardner/hdfs/stispaper>.

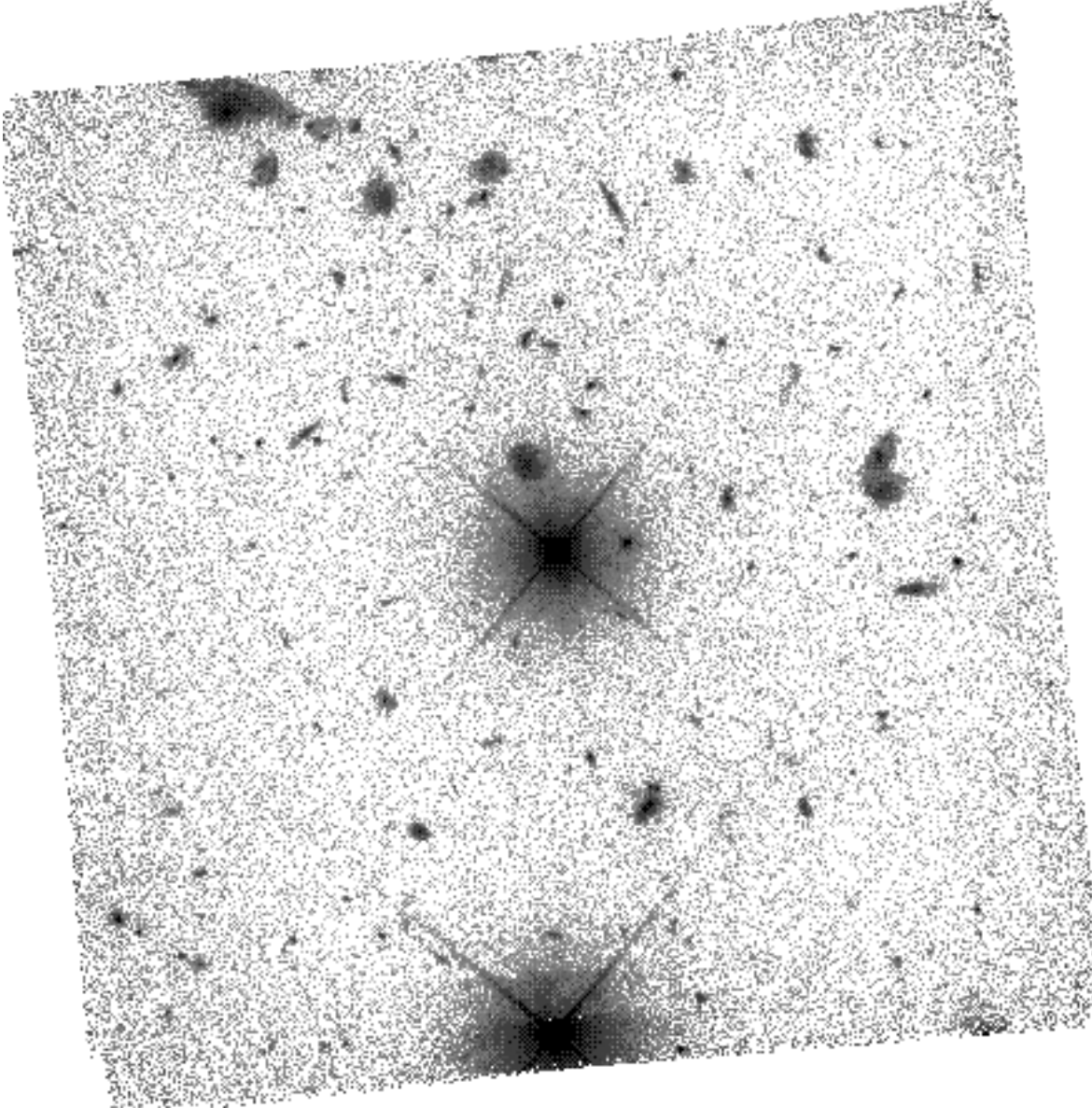


Fig. 1.— The 50CCD image. The image is displayed on a log scale, and has been clipped between  $1 \times 10^{-5}$  and  $5 \times 10^{-2}$  counts per second. The field of view of the image is 0.8357 square arcminutes.

NOTE: The resolution of this image has been reduced. Full resolution images are available at: <http://hires.gsfc.nasa.gov/~gardner/hdfs/stispaper>.

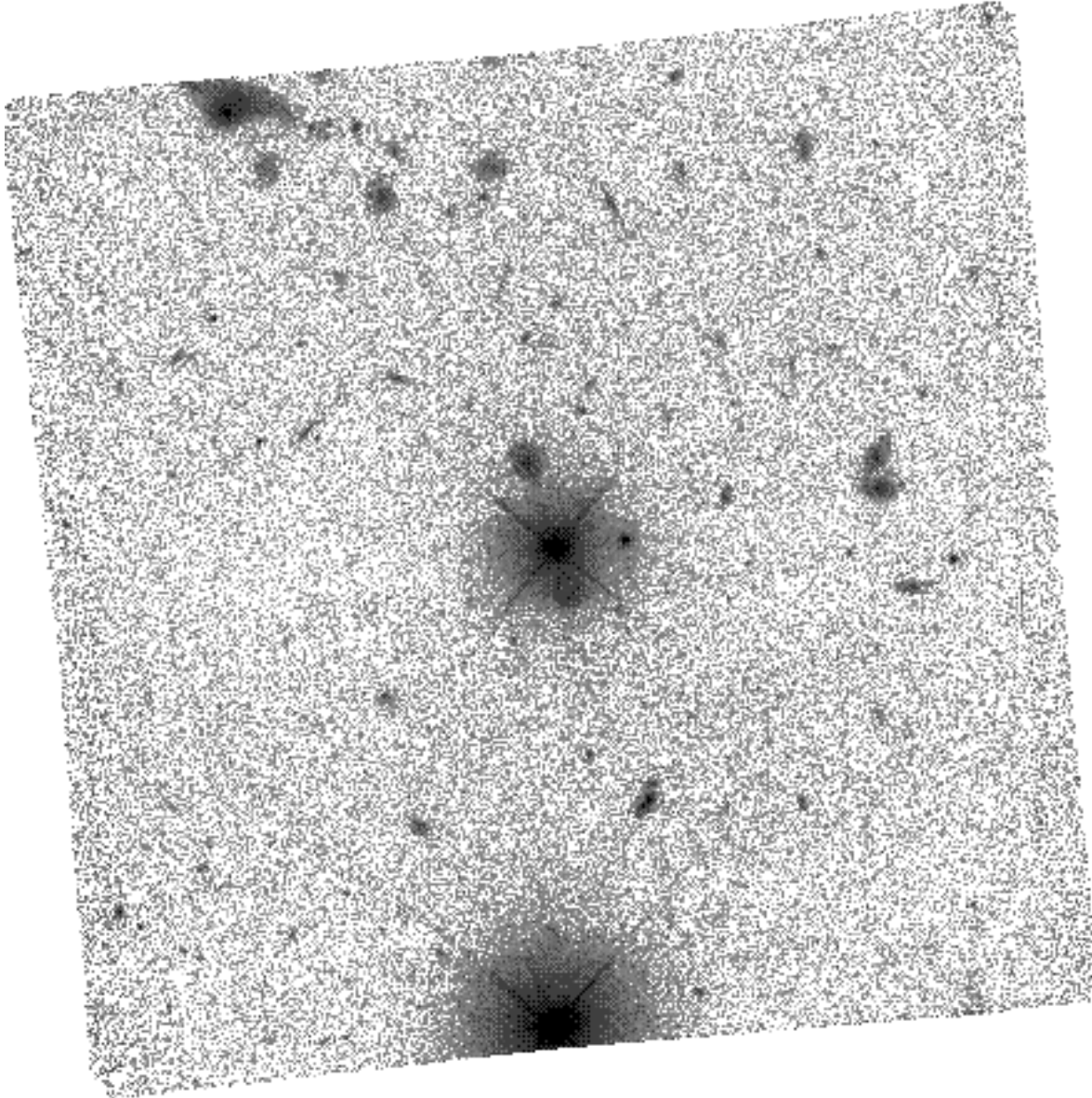


Fig. 2.— The F28X50LP image. The image is displayed on a log scale, and has been clipped between  $1 \times 10^{-5}$  and  $5 \times 10^{-2}$  counts per second. The field of view of the image is 0.8326 square arcminutes.

NOTE: The resolution of this image has been reduced. Full resolution images are available at: <http://hires.gsfc.nasa.gov/~gardner/hdfs/stispaper>.

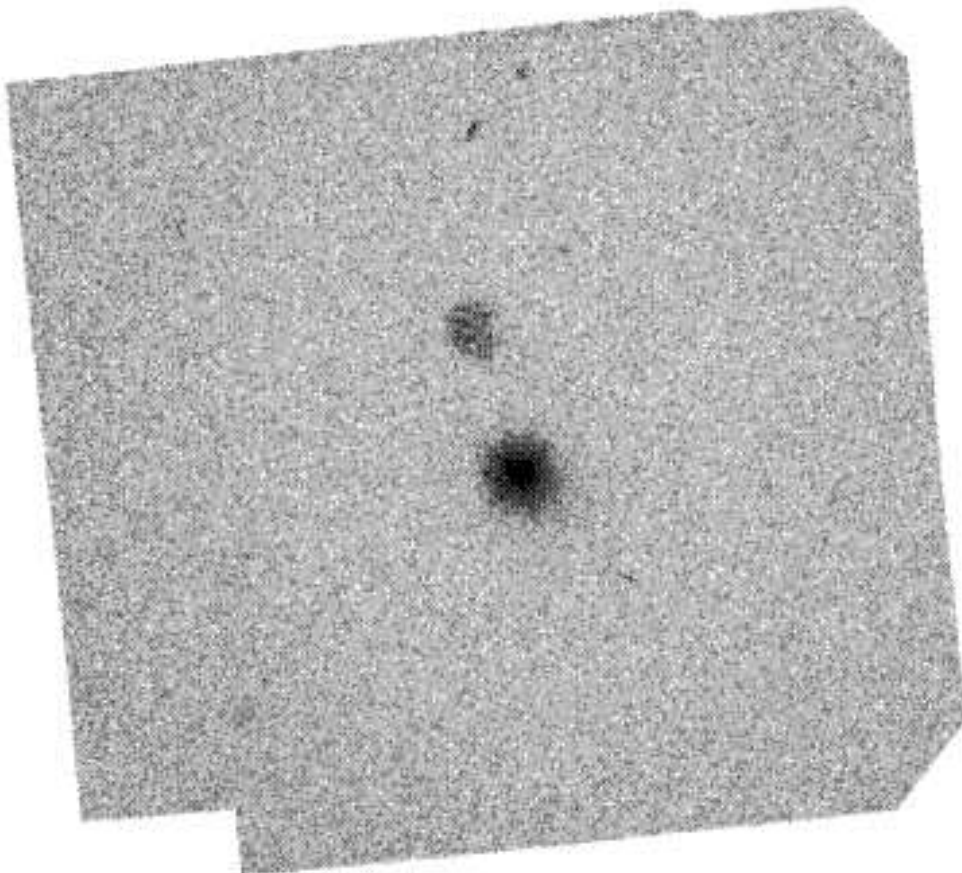


Fig. 3.— The NUVQTZ image. The image is displayed on a log scale, and has been clipped between  $1 \times 10^{-6}$  and  $5 \times 10^{-3}$  counts per second, and has been smoothed with a  $5 \times 5$  pixel box average. The field of view of the image is 0.2221 square arcminutes.

NOTE: The resolution of this image has been reduced. Full resolution images are available at: <http://hires.gsfc.nasa.gov/~gardner/hdfs/stispaper>.

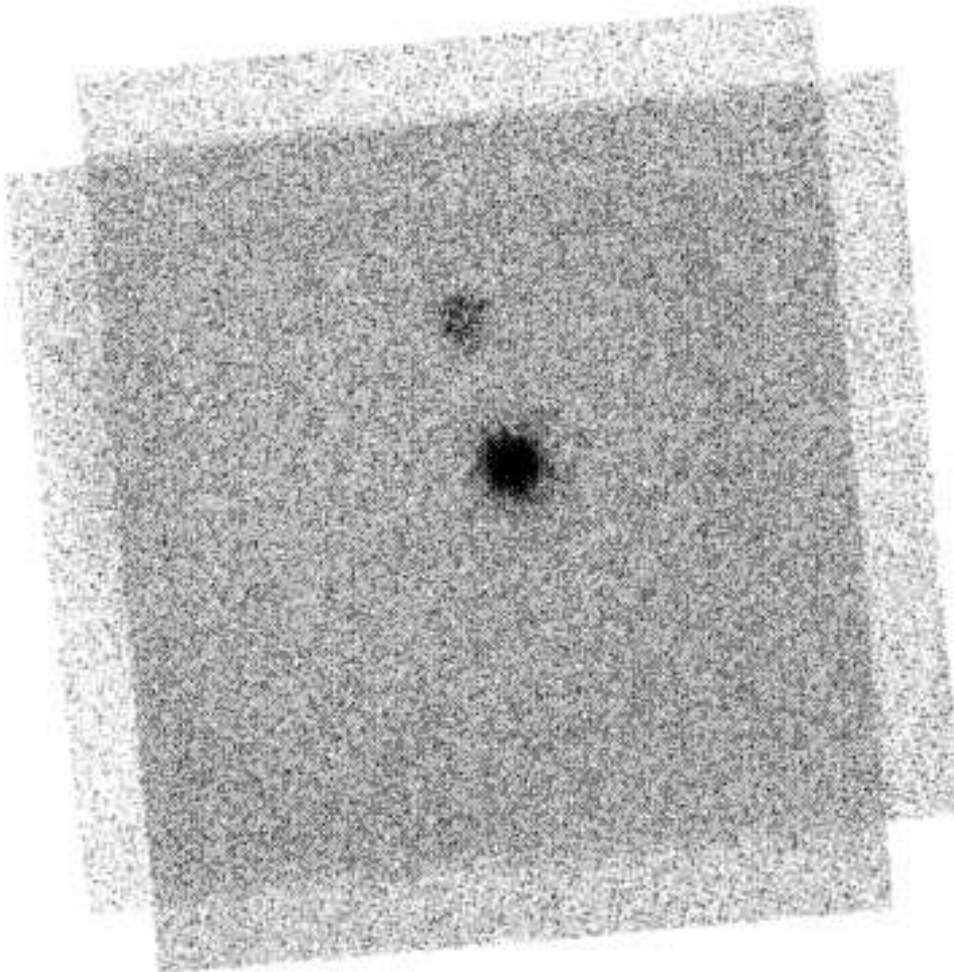


Fig. 4.— The FUVQTZ image. The image is displayed on a log scale, and has been clipped between  $1 \times 10^{-8}$  and  $5 \times 10^{-5}$  counts per second, and has been smoothed with a  $5 \times 5$  pixel box average. The field of view of the image is 0.2438 square arcminutes.

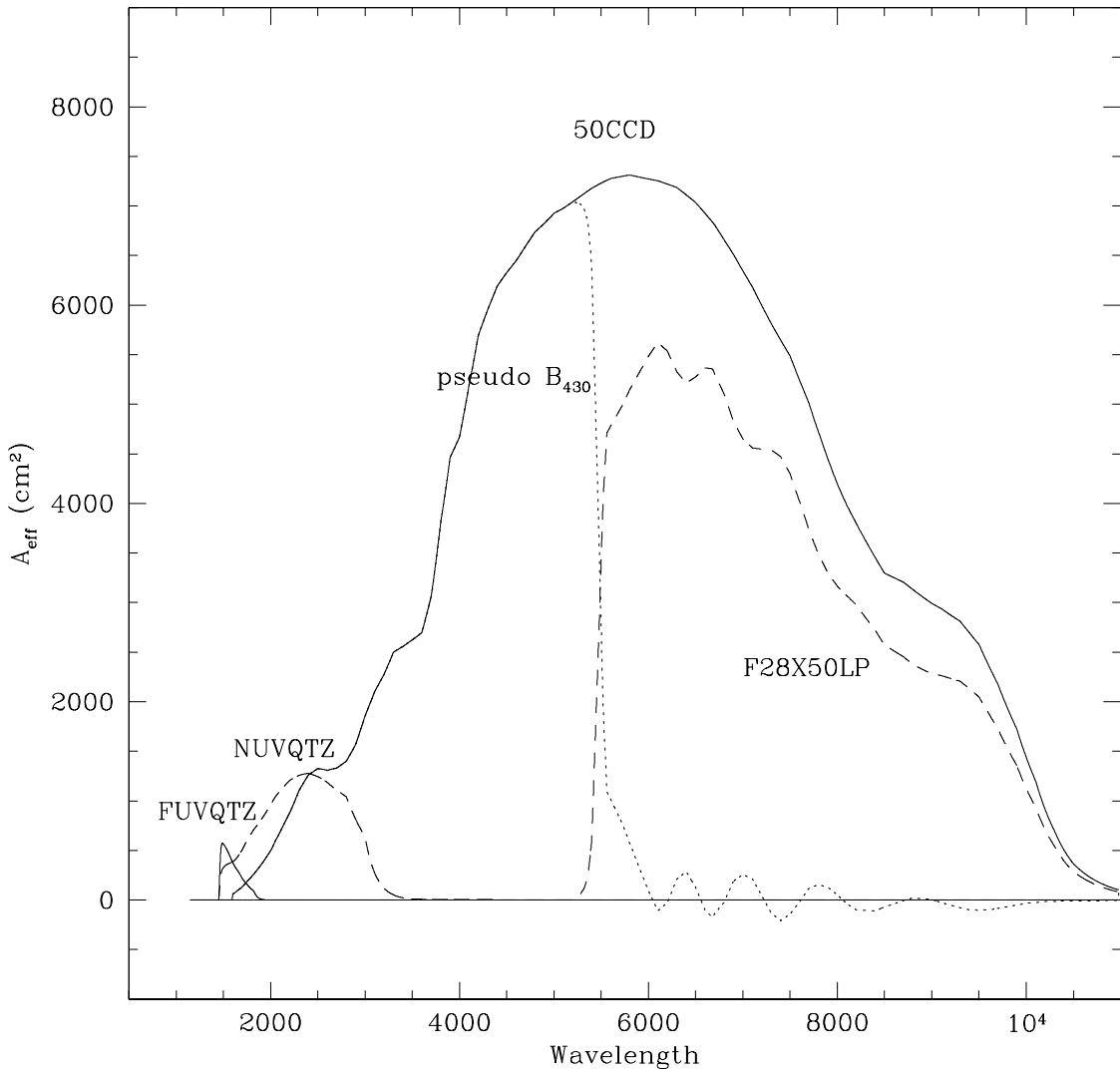


Fig. 5.— Effective areas of the 4 imaging modes. The 50CCD mode is filterless imaging with a CCD, and this curve represents the response of the detector. The other three modes are a combination of the throughput of the filter with the response functions of the CCD and the two MAMA detectors. Also plotted is a pseudo- $B_{430}$  bandpass, constructed from the fluxes by 50CCD - 1.31(F28X50LP).

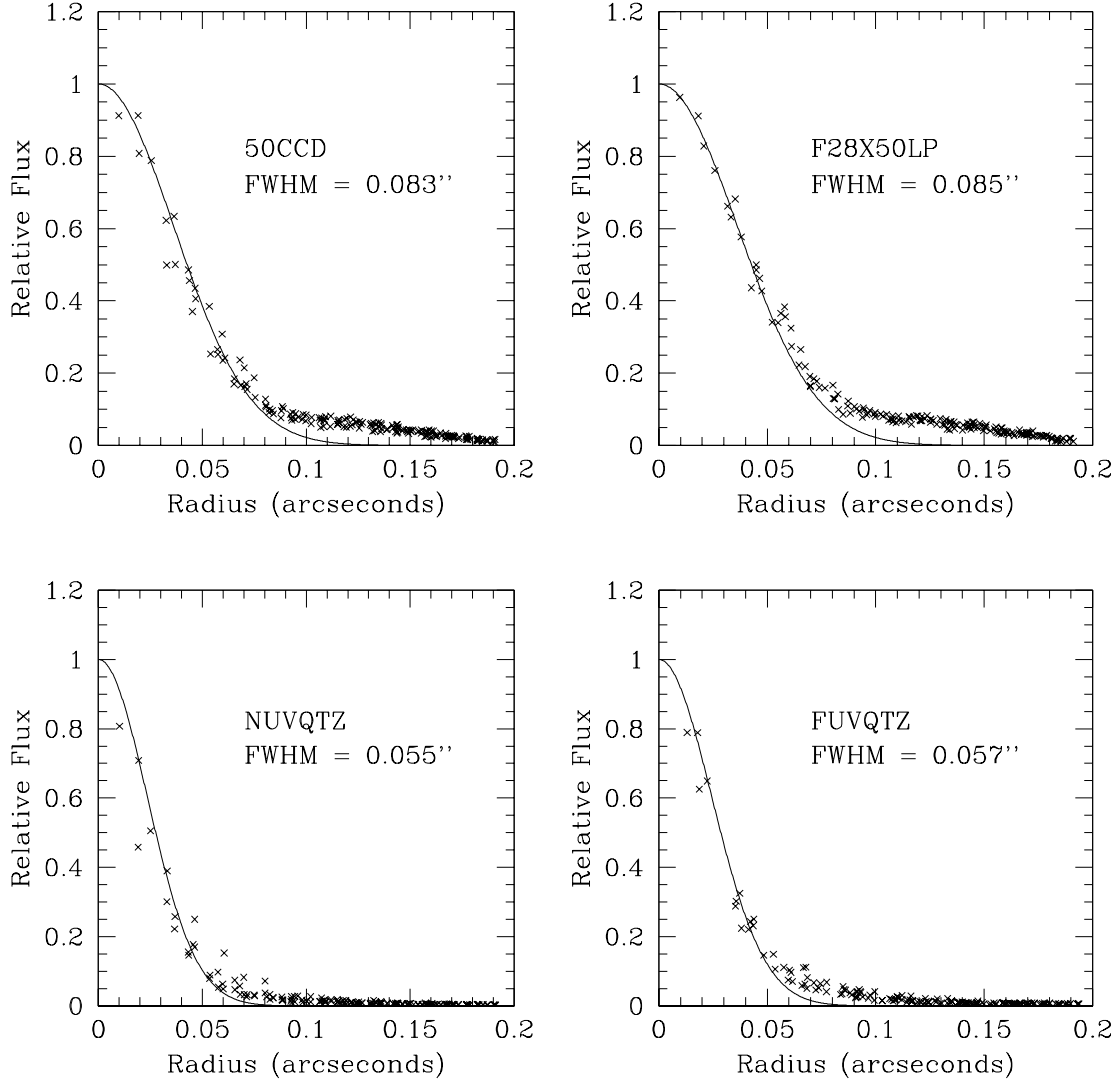


Fig. 6.— Point spread functions of the final images. The points plotted are each pixel value as a function of distance from the centroid of the point source. The lines are a Gaussian with the same full width half maximum as the PSF. The objects plotted are the red point source just to the west of the quasar in the optical images, and the quasar itself in the ultraviolet images.

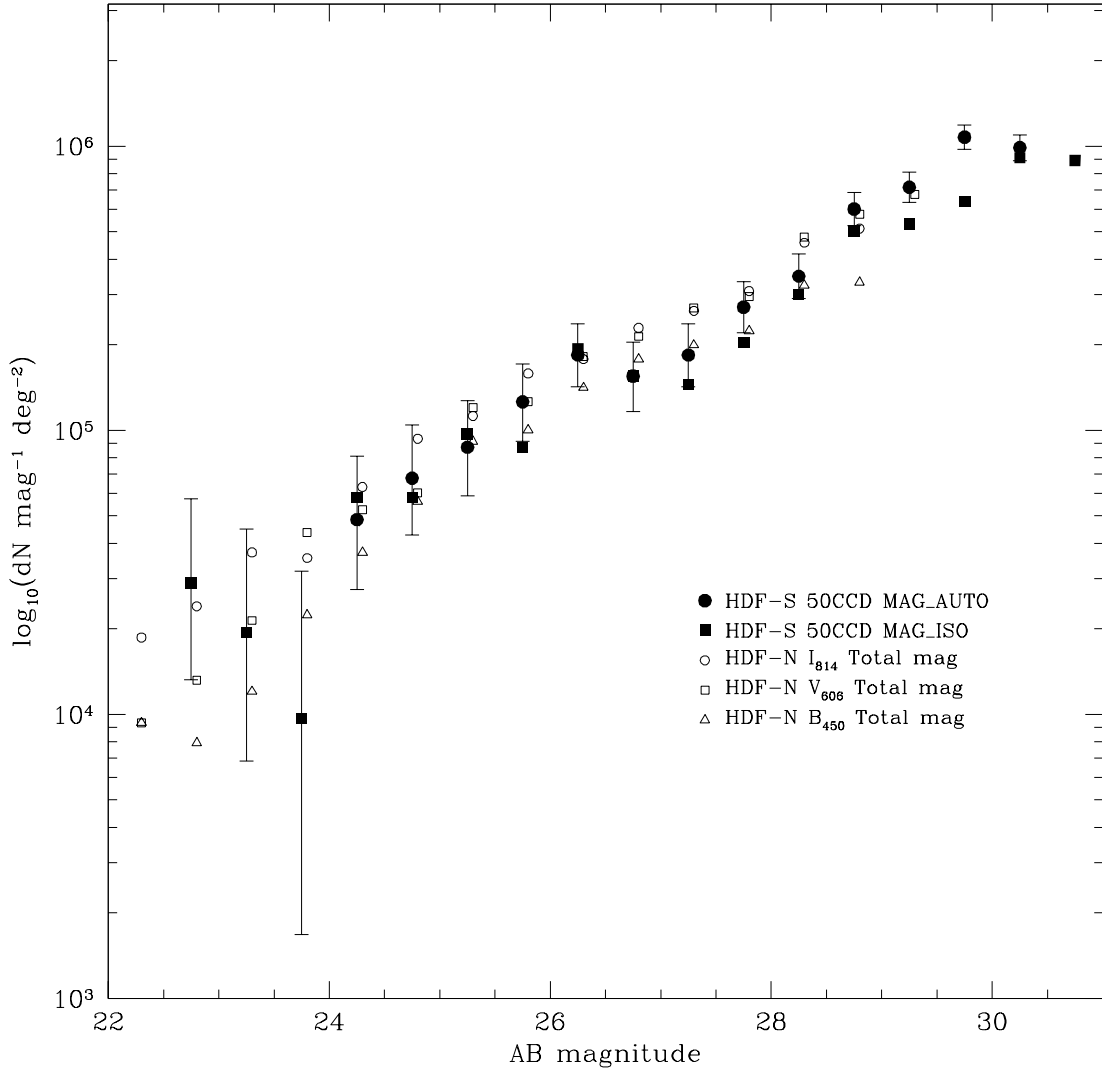


Fig. 7.— The source counts in the 50CCD image scaled to objects per square degree per magnitude as a function of AB magnitude. We plot both the MAG\_AUTO and MAG\_ISO counts, binned at different magnitudes to show the points. We plot Poissonian errors on the points. For comparison, we plot the WFPC2 HDF-N galaxy counts, in  $B_{450}$ ,  $V_{606}$ , and  $I_{814}$ , based upon the total magnitude as given by Williams et al. (1996). The error bars reflect  $\sqrt{N}$  counting statistics and do not include systematic errors in the photometry or galaxy clustering.

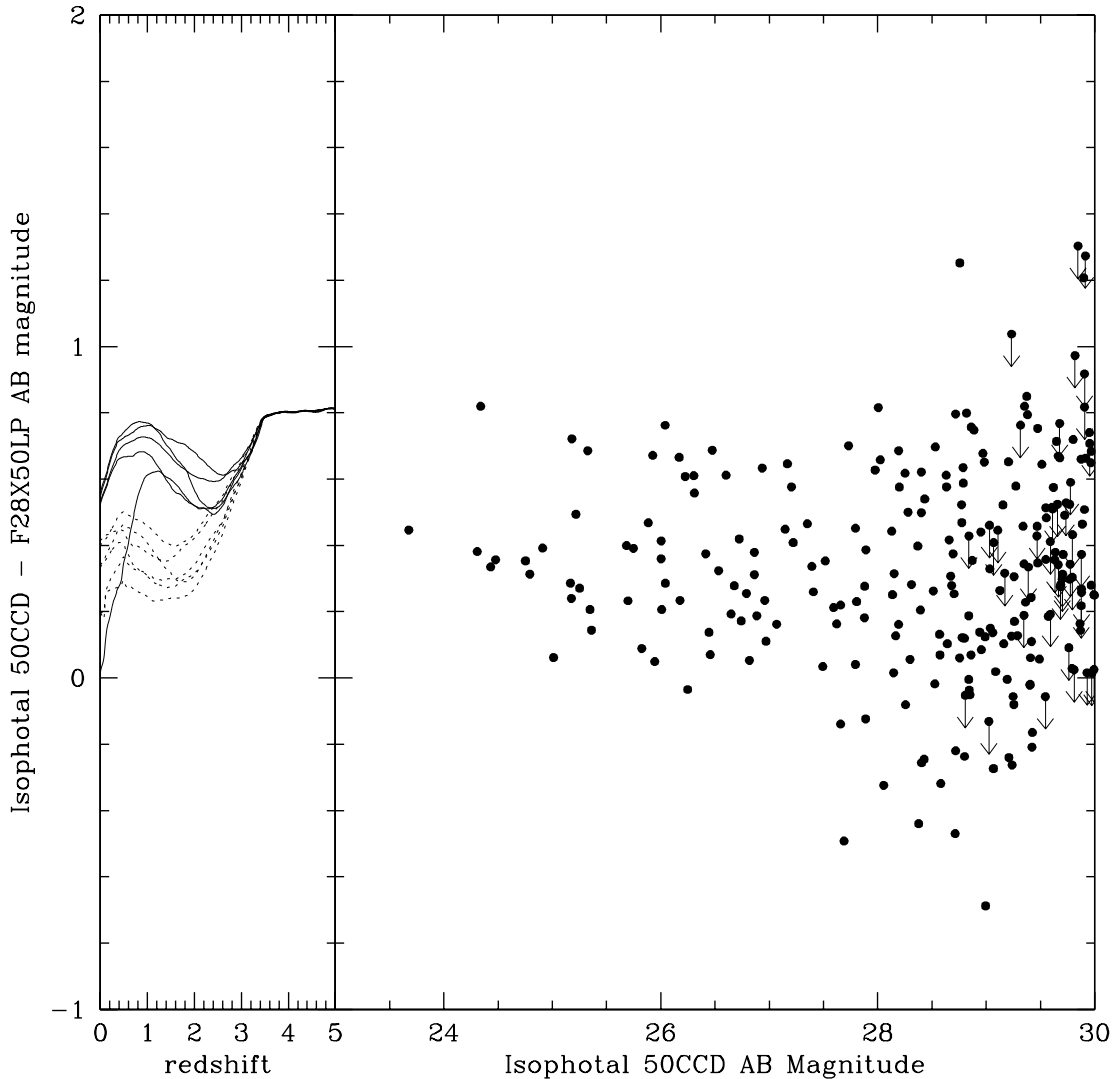


Fig. 8.— 50CCD-F28X50LP AB magnitudes plotted as a function of 50CCD magnitude. The magnitudes and colors are isophotal. On the left we plot the K-corrected colors of the template galaxies in the Kinney et al. (1996) sample as a function of redshift. The “normal” galaxies from that sample are plotted as solid lines, and the starburst galaxies are plotted as dotted lines. The templates do not include data shortward of Ly $\alpha$ , so the plots converge when this limit is redshifted into the F28X50LP filter. In real high-z galaxies, a similar effect would be caused by the Ly $\alpha$  forest.

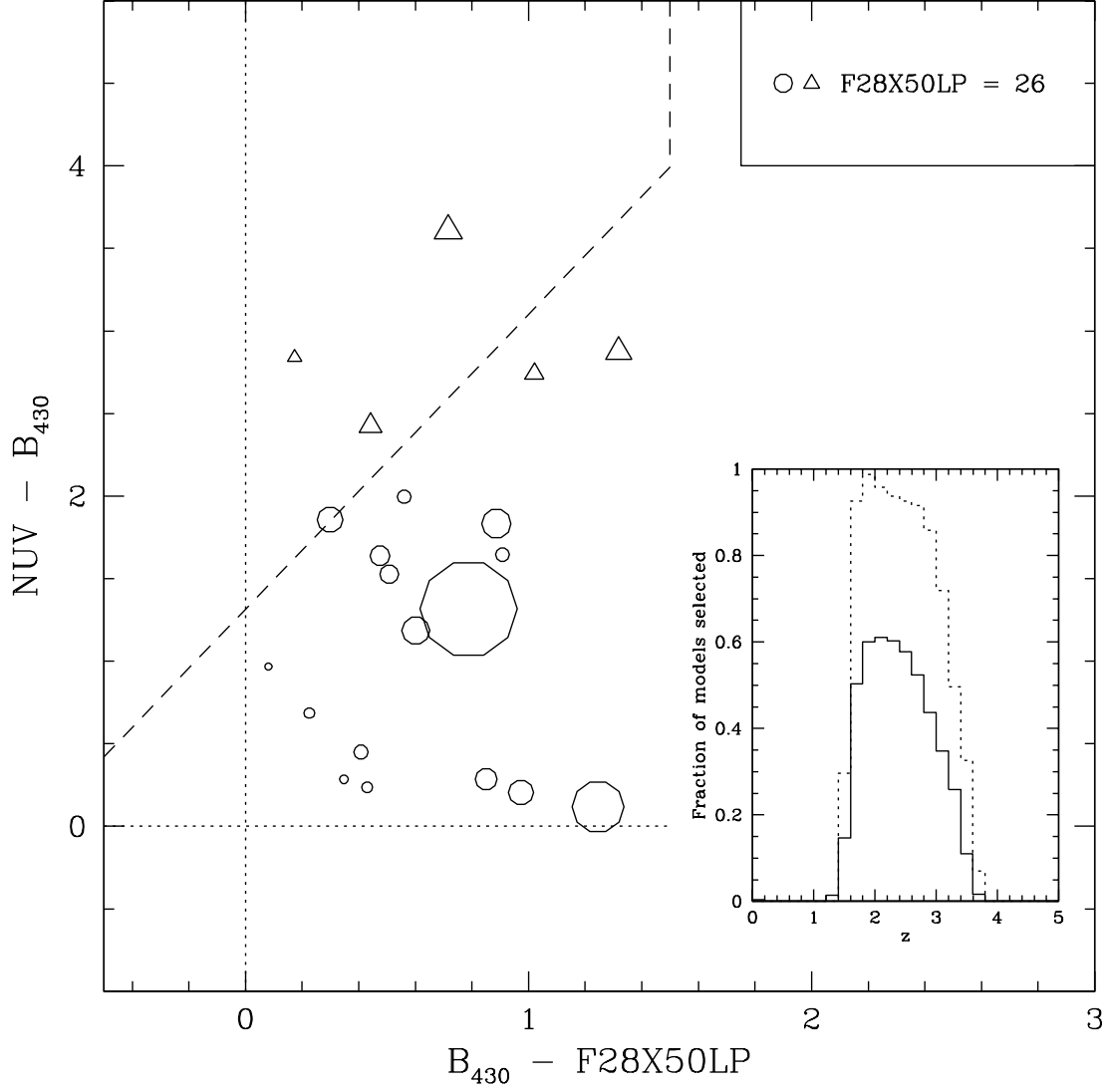


Fig. 9.— A color-color plot of the STIS NUV -  $B_{430}$  vs.  $B_{430}$  - F28X50LP, where  $B_{430}$  is a pseudo bandpass obtained by subtracting a scaled F28X50LP flux from the 50CCD flux. The dashed line shows the selection boundary for objects with  $1.5 < z < 3.5$ . The size of the symbols indicates their magnitudes, and the symbol size of an object with  $F28X50LP = 26$  is indicated in the inset at the upper right. Circular symbols are detected at the 1 sigma level in all bands, while triangles are undetected in the NUV, providing lower limits to the color. In the inset figure at right, we plot the selection efficiency of the NUV drop-out technique. This shows the fraction of models from the Madau et al. (1996) grid meeting the color selection criteria. The selection criteria are  $NUV - B_{430} > 1.75(B_{430} - F28X50LP) + 1.3$ , AND  $B_{430} - F28X50LP < 1.5$ . The solid line is the full set of models (including old and highly reddened galaxies). The dotted line is just those model galaxies with ages  $< 10^8$  years and foreground-screen extinction less than  $A_B = 2$ .

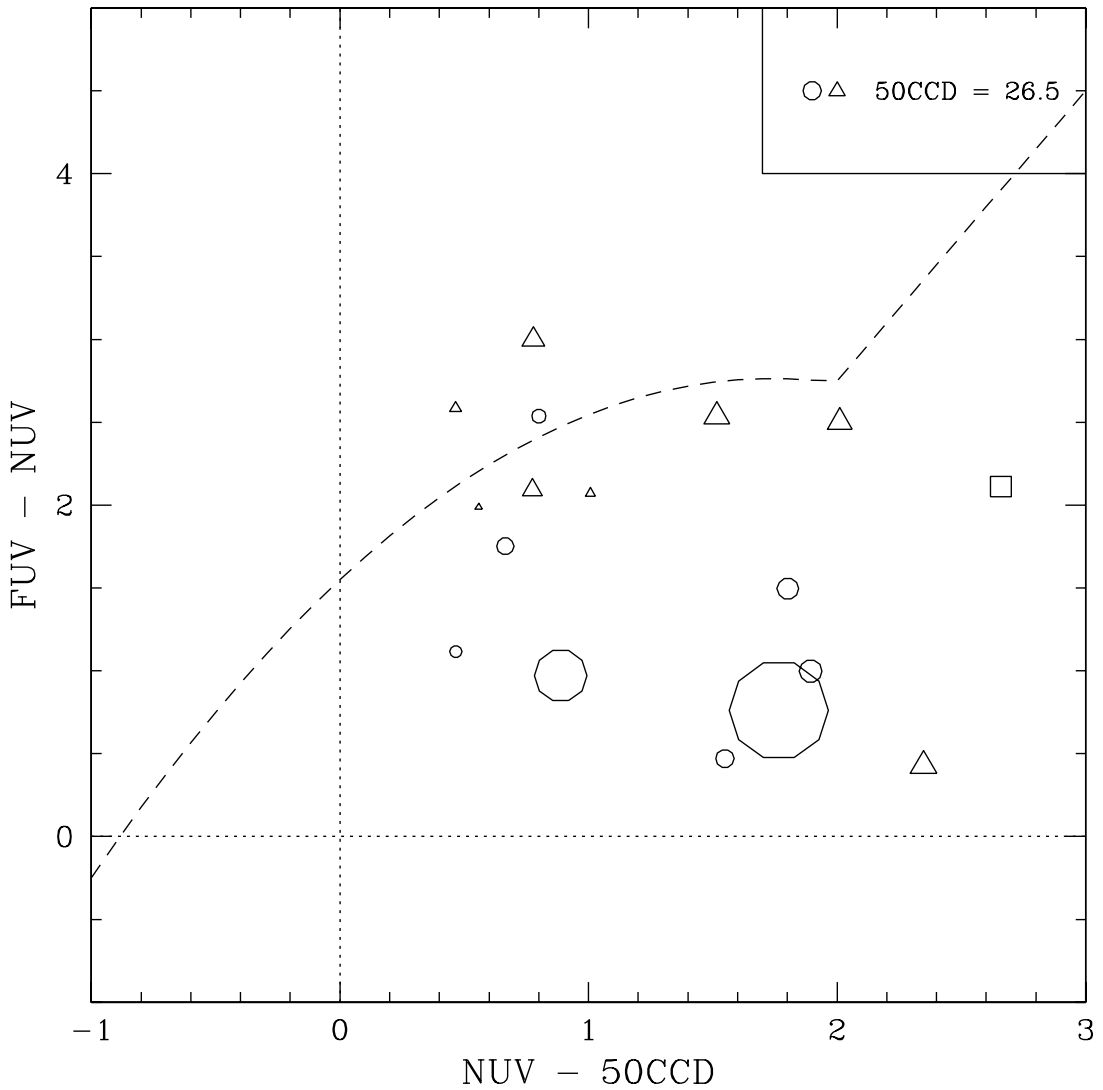


Fig. 10.— A color-color plot of the STIS FUV - NUV vs. NUV - 50CCD. The dashed line shows the selection boundary for objects with  $0.6 < z < 1.5$ . The symbols are as in Figure 9; in addition, the square symbols represent objects which are not detected at the  $1\sigma$  level in either the NUV or the FUV.

Table 1. Description of the Observations

Mode	Central Wavelength	Width	Detector FOV	Total Exposure	Depth	Resolution
FUVQTZ	1590 Å	220 Å	25'' × 25''	52124 sec	27.8	0.057''
NUVQTZ	2320 Å	1010 Å	25'' × 25''	22616 sec	27.5	0.055''
50CCD	5850 Å	4410 Å	52'' × 52''	155590 sec	29.4	0.083''
F28X50LP	7230 Å	2720 Å	28'' × 52''	49768 sec	27.5	0.085''

Note. — The detector fields of view have been clipped slightly to remove vignetting. The total exposure time for the F28X50LP mode is split into two fields of view with 23202 seconds exposure in the southern half, 25806 sec exposure in the northern half, and 760 seconds exposure in the central part of the field. The observations overlap, so that the region containing the QSO has full exposure. Depths are AB magnitudes at  $10\sigma$  in a 0.2 square arcsecond aperture for the deepest part of the image. The resolution given is the full-width-half-maximum of point sources, as shown in Figure 6

Table 2. The catalog

ID	HDFS_J22r-60d	x	y	$m_i$	$m_a$	clr-lp	nuv-clr	fuv-clr	$r_h$	s/g	flags
552	3333.69	3346.0	2354.86	530.80	28.73	27.71	-0.11	...	175	0.21	adehkn
576	3333.81	3347.3	2320.27	479.99	29.03	28.90	<0.46	...	69	0.12	ekn
491	3333.91	3341.2	2292.26	723.83	30.91	29.89	<1.43	...	95	0.97	ekn
531	3333.91	3343.9	2292.27	615.84	30.68	30.01	<1.04	...	85	0.98	hkn
572	3333.93	3346.9	2284.00	493.81	30.76	30.22	<0.70	...	73	0.96	kn
419	3333.97	3336.4	2275.12	916.66	27.07	27.11	0.16	...	121	0.03	ekn
650	3333.99	3353.6	2268.43	226.34	30.76	30.23	0.52	...	55	0.89	ehkn
293	3334.08	3327.6	2241.08	1265.37	30.13	30.02	<0.70	...	57	0.59	kn
278	3334.12	3323.7	2230.81	1424.99	28.85	28.88	-0.05	...	51	0.85	ehkn
345	3334.13	3331.2	2227.79	1122.83	30.01	29.55	<0.77	...	79	0.66	kn
454	3334.13	3338.9	2227.56	816.29	30.23	29.43	<0.96	...	148	0.78	kn
557	3334.13	3346.0	2226.26	531.39	31.65	30.63	<1.17	...	74	0.81	kn
600	3334.17	3350.1	2213.57	367.28	31.42	30.17	<0.85	...	117	0.76	kn
287	3334.18	3327.3	2212.17	1279.84	29.41	29.09	0.06	...	91	0.06	kn
153	3334.20	3316.4	2206.50	1713.55	28.76	28.73	1.25	...	83	0.02	ekn
476	3334.20	3340.5	2206.71	752.90	31.28	30.80	<1.18	...	60	0.90	kn
67	3334.23	3309.4	2197.32	1995.20	30.86	31.43	<1.26	...	26	0.94	ekn
504	3334.24	3342.2	2194.78	683.83	28.01	27.83	0.82	...	117	0.02	kn
368	3334.25	3333.1	2190.29	1045.95	30.25	29.44	<1.15	...	136	0.07	kn
627	3334.29	3352.3	2179.91	280.70	31.27	30.31	<0.74	...	65	0.88	kn
652	3334.30	3348.3	2175.89	439.09	31.57	31.11	<0.90	...	46	0.77	kn
366	3334.34	3332.6	2163.37	1065.86	31.41	30.48	<1.38	...	88	0.86	kn
110	3334.35	3312.7	2160.87	1861.57	30.50	30.13	1.22	...	58	0.96	hkn
35	3334.36	3306.2	2159.44	2122.56	29.90	29.60	0.51	...	87	0.52	kn
448	3334.37	3338.2	2156.12	841.93	29.57	28.99	0.19	...	128	0.01	kn
688	3334.39	3300.2	2150.41	2361.54	26.18	25.66	0.27	...	143	0.25	adehkn
565	3334.41	3346.5	2143.93	510.94	28.84	28.78	0.19	...	61	0.78	kn
172	3334.42	3317.3	2141.37	1680.09	29.47	29.19	0.43	...	98	0.04	kn
439	3334.43	3337.4	2137.45	875.82	30.42	30.31	<0.28	...	52	0.81	kn
644	3334.44	3355.0	2133.56	172.93	24.47	23.60	-1.56	...	375	0.03	abehkn
200	3334.45	3318.9	2133.51	1616.24	28.43	28.31	-0.25	...	107	0.02	kn
625	3334.45	3352.1	2131.66	287.95	30.86	29.93	<0.99	...	96	0.96	kn
409	3334.46	3335.5	2128.74	949.42	31.52	30.06	1.06	...	118	0.89	kn
591	3334.48	3349.9	2124.37	377.26	28.19	28.02	0.69	...	151	0.02	kn
643	3334.49	3353.6	2120.62	229.30	26.60	24.64	0.43	...	1641	0.03	abehkn
118	3334.50	3314.2	2118.99	1801.42	25.70	25.58	0.23	...	348	0.03	kn
546	3334.50	3345.5	2116.83	552.59	30.09	30.10	<0.35	...	65	0.12	kn
647	3334.50	3348.5	2117.43	431.79	26.25	26.26	-0.03	...	76	0.76	kn
521	3334.52	3343.1	2111.12	647.07	30.41	29.91	<0.67	...	155	0.15	kn
286	3334.53	3327.4	2107.82	1275.49	26.74	26.70	0.17	...	132	0.03	kn
571	3334.53	3347.0	2108.80	493.06	28.68	28.57	0.28	...	93	0.04	kn
435	3334.54	3337.0	2106.43	890.93	31.24	29.55	0.85	...	175	0.86	kn
637	3334.54	3352.7	2106.20	261.96	29.76	29.18	<0.09	...	110	0.23	kn
21	3334.55	3304.8	2102.49	2178.34	29.42	29.03	-0.21	...	79	0.82	kn
66	3334.55	3309.1	2104.17	2008.66	29.15	28.84	0.52	...	138	0.01	kn
554	3334.57	3346.0	2097.22	531.69	30.59	30.17	0.45	...	84	0.79	kn
577	3334.59	3259.8	2089.82	2378.98	28.63	27.71	0.02	...	88	0.95	dehkn
217	3334.59	3320.2	2090.39	1562.33	29.47	28.89	0.75	...	147	0.01	kn
340	3334.61	3331.0	2083.86	1131.74	30.62	30.02	<1.10	...	100	0.74	kn
210	3334.62	3319.9	2081.06	1575.17	30.60	29.72	0.88	...	109	0.25	akn
319	3334.65	3329.7	2074.17	1182.91	24.34	24.37	0.82	...	64	0.98	kn
194	3334.68	3319.5	2064.18	1591.88	28.46	27.88	0.22	...	193	0.02	abkn

Table 2—Continued

ID	HDFS_J22r-60d	x	y	$m_i$	$m_a$	clr-lp	nuv-clr	fuv-clr	$r_h$	s/g	flags
39	3334.69	3306.4	2062.38	2115.16	30.40	30.31	0.39	...	61	0.76	kn
407	3334.69	3335.5	2061.73	950.35	28.72	28.66	0.80	...	74	0.39	kn
151	3334.71	3316.2	2057.00	1724.42	31.59	31.18	<1.44	...	49	0.82	kn
537	3334.73	3344.8	2049.93	580.21	29.91	29.60	<0.82	...	114	0.01	kn
193	3334.74	3319.0	2046.89	1612.56	28.29	27.26	-0.01	...	522	0.00	bkn
381	3334.77	3333.6	2038.35	1027.26	31.23	29.96	<1.20	...	135	0.90	kn
489	3334.78	3341.0	2034.33	729.71	31.60	31.31	0.94	...	44	0.86	kn
305	3334.81	3328.6	2025.49	1226.92	29.63	29.50	<0.36	...	89	0.16	kn
316	3334.84	3329.1	2015.84	1206.72	31.11	30.34	<1.15	...	88	0.90	kn
472	3334.84	3340.3	2016.13	759.59	31.15	30.80	<0.94	...	65	0.92	kn
606	3334.85	3350.8	2013.56	339.75	27.88	27.71	0.18	...	139	0.03	kn
219	3334.87	3320.7	2009.03	1544.97	26.30	26.29	0.61	...	113	0.03	kn
375	3334.87	3333.4	2007.04	1033.79	30.79	30.38	<1.26	...	107	0.41	kn
615	3334.87	3351.2	2007.40	322.97	31.07	30.57	<0.54	...	59	0.95	akn
295	3334.88	3327.7	2004.25	1264.65	31.48	31.05	<0.49	...	63	0.81	kn
418	3334.88	3336.2	2004.32	925.16	31.78	30.81	<1.01	...	86	0.77	kn
613	3334.89	3351.1	2001.05	329.15	30.13	29.81	0.56	...	82	0.48	akn
447	3334.91	3338.1	1997.04	849.33	29.03	28.95	<-0.13	...	61	0.82	kn
18	3334.94	3304.8	1986.64	2181.27	29.95	29.71	0.74	...	82	0.25	kn
86	3334.94	3310.9	1987.52	1936.48	29.67	29.46	0.67	...	91	0.02	kn
227	3334.94	3320.9	1986.43	1534.93	30.85	30.17	0.67	...	106	0.48	akn
585	3334.94	3349.2	1986.74	403.84	30.37	29.95	<0.23	...	74	0.95	kn
335	3334.95	3331.2	1983.88	1123.76	24.31	24.29	0.38	...	386	0.03	kn
325	3334.96	3329.8	1981.73	1179.54	31.45	31.08	<1.58	...	51	0.92	kn
596	3334.96	3350.0	1981.11	373.15	30.27	29.99	0.40	...	94	0.15	kn
85	3335.00	3308.7	1969.95	2022.72	30.81	30.09	<1.29	...	111	0.45	kn
651	3335.01	3353.8	1966.30	219.85	29.55	29.32	<-0.06	...	74	0.81	kn
44	3335.02	3307.2	1963.48	2084.38	28.31	27.95	0.16	...	152	0.02	abkn
202	3335.02	3319.1	1964.16	1607.11	29.55	29.30	0.48	...	99	0.03	kn
43	3335.05	3307.0	1954.77	2091.07	28.47	28.27	0.40	...	105	0.02	abkn
61	3335.05	3308.3	1956.41	2038.86	30.72	30.10	<0.88	...	91	0.44	kn
611	3335.05	3352.3	1954.88	279.42	28.11	27.87	-0.12	...	106	0.03	abkn
672	3335.06	3348.4	1952.76	434.94	31.08	30.84	<0.68	...	64	0.64	kn
185	3335.07	3317.9	1950.30	1656.38	29.51	29.27	0.64	...	71	0.20	kn
542	3335.07	3345.3	1949.22	557.86	31.13	30.44	<1.20	...	93	0.92	kn
137	3335.08	3315.3	1945.67	1759.58	26.82	26.76	0.05	...	235	0.03	kn
490	3335.08	3341.2	1946.35	722.51	28.81	28.63	<-0.05	...	115	0.01	kn
475	3335.09	3340.5	1944.33	751.19	28.94	28.78	0.14	...	126	0.01	kn
610	3335.09	3351.4	1943.56	316.90	26.59	26.36	-0.15	...	295	0.03	bkn
242	3335.10	3318.2	1941.78	1643.60	30.80	30.48	<1.16	...	63	0.78	kn
92	3335.12	3311.6	1934.06	1909.17	31.58	30.65	<1.17	...	74	0.83	kn
234	3335.15	3321.6	1926.94	1508.92	29.09	29.07	0.02	...	77	0.02	kn
245	3335.19	3325.9	1912.74	1336.84	23.41	23.36	0.51	...	544	0.03	abkn
441	3335.19	3338.2	1913.07	843.58	25.93	25.85	0.67	...	315	0.03	kn
187	3335.20	3318.1	1911.98	1649.17	28.38	28.27	-0.44	...	116	0.02	kn
327	3335.21	3330.1	1907.49	1166.09	29.35	29.00	0.82	...	99	0.02	kn
426	3335.21	3336.9	1906.65	893.69	30.21	29.88	<0.58	...	101	0.31	abkn
41	3335.22	3307.1	1904.44	2086.71	26.86	26.80	0.31	...	168	0.03	kn
288	3335.22	3324.2	1905.53	1403.51	23.49	23.40	0.42	...	537	0.03	abkn
298	3335.23	3327.9	1903.49	1254.11	31.21	30.62	<0.98	...	81	0.93	kn
425	3335.23	3336.7	1900.88	903.79	29.68	29.15	<0.59	...	152	0.00	abkn
420	3335.24	3336.3	1899.75	920.25	30.65	29.70	0.62	...	140	0.13	akn

Table 2—Continued

ID	HDFS_J22r-60d	x	y	$m_i$	$m_a$	clr-lp	nuv-clr	fuv-clr	$r_h$	s/g	flags	
291	3335.28	3327.7	1887.55	1262.31	28.86	28.69	0.76	...	105	0.02	kn	
477	3335.30	3340.5	1882.17	751.06	31.44	30.64	<0.95	...	76	0.82	kn	
364	3335.31	3332.7	1877.23	1063.65	28.62	28.59	0.12	...	65	0.38	abkn	
365	3335.32	3333.2	1874.77	1043.81	28.40	28.28	0.31	...	95	0.02	abkn	
461	3335.32	3339.4	1876.55	796.37	31.28	31.15	<0.73	...	47	0.90	kn	
70	3335.38	3309.8	1858.29	1978.24	30.57	30.18	<0.89	...	66	0.86	kn	
620	3335.38	3351.7	1858.82	304.05	30.00	30.41	0.25	...	55	0.97	kn	
487	3335.41	3341.1	1848.95	727.26	27.66	27.64	-0.14	...	83	0.04	kn	
317	3335.42	3329.4	1847.33	1196.27	26.41	26.41	0.37	...	106	0.04	kn	
338	3335.42	3330.9	1846.76	1135.23	29.66	29.17	<0.34	...	127	0.01	kn	
223	3335.44	3320.7	1841.36	1543.56	30.50	29.66	<0.63	...	128	0.02	kn	
626	3335.45	3348.0	1836.68	450.26	28.14	28.03	0.25	...	193	0.00	kn	
412	3335.50	3335.2	1822.64	964.45	28.26	28.10	-0.08	...	112	0.03	kn	
446	3335.51	3338.0	1818.46	850.97	30.10	29.96	<0.70	...	77	0.19	kn	
149	3335.52	3316.1	1816.45	1725.55	31.60	31.26	<0.85	...	49	0.86	kn	
281	3335.53	3322.8	1813.72	1460.07	28.70	28.54	0.25	...	173	0.00	kn	
274	3335.54	3325.9	1809.67	1337.02	30.07	29.92	0.45	...	122	0.15	bkn	
189	3335.55	3318.2	1807.28	1643.69	26.53	26.53	0.32	...	140	0.03	kn	
162	3335.57	3316.8	1803.18	1699.17	31.12	30.38	<1.27	...	92	0.90	kn	
199	3335.57	3318.7	1802.69	1623.57	31.79	31.29	<1.42	...	49	0.74	kn	
355	3335.57	3324.4	1802.11	1394.03	31.16	30.84	<0.75	...	68	0.86	kn	
275	3335.57	3326.0	1800.73	1331.60	30.47	30.34	<0.74	...	85	0.16	abkn	
159	3335.59	3316.6	1794.94	1706.89	31.60	30.49	<1.64	...	95	0.81	akn	
105	3335.64	3313.1	1782.55	1848.08	26.01	25.97	0.21	...	224	0.03	kn	
277	3335.70	3326.0	1762.65	1333.04	29.62	29.25	0.58	>-0.68	...	102	0.01	ln
346	3335.70	3330.8	1764.00	1137.55	29.16	28.91	0.10	>-0.21	>0.19	113	0.01	
503	3335.70	3342.0	1764.28	692.79	30.99	30.47	<1.06	...	86	0.84	kn	
692	3335.71	3302.0	1760.29	2292.15	30.97	30.77	<0.19	...	43	0.88	kn	
455	3335.71	3338.9	1761.54	817.02	32.13	31.19	<1.45	...	>-1.51	61	0.67	k
154	3335.73	3316.5	1755.73	1712.69	29.39	29.29	<0.33	...	95	0.03	kn	
192	3335.73	3318.3	1753.83	1640.63	29.35	29.28	<0.19	...	89	0.01	kn	
75	3335.74	3310.1	1751.50	1968.62	31.05	30.41	<0.60	...	73	0.93	kn	
283	3335.74	3326.7	1751.98	1302.21	29.47	29.24	0.35	>-0.30	>-0.13	83	0.09	
566	3335.74	3346.7	1752.61	501.73	30.74	30.37	0.88	...	65	0.82	kn	
34	3335.75	3307.2	1747.64	2083.59	24.48	24.45	0.36	...	439	0.03	kn	
104	3335.75	3312.4	1748.77	1875.44	30.48	29.76	<0.42	...	117	0.18	kn	
635	3335.76	3352.7	1746.81	265.36	31.02	30.82	<0.68	...	64	0.79	kn	
509	3335.77	3343.0	1743.06	652.60	25.01	24.99	0.06	...	>6.55	260	0.03	ko
228	3335.78	3321.1	1739.34	1528.22	28.99	29.12	-0.05	>-1.42	>-0.06	153	0.00	alo
474	3335.83	3340.7	1723.84	744.28	29.50	29.34	0.37	...	>0.14	84	0.04	abk
88	3335.84	3311.2	1721.11	1921.99	28.76	28.56	0.06	...	120	0.18	kn	
640	3335.84	3353.0	1720.97	250.97	28.57	28.22	0.13	...	196	0.02	kn	
284	3335.85	3326.7	1719.83	1302.44	30.89	30.56	0.85	>-0.97	>-0.75	68	0.96	
623	3335.85	3352.0	1720.19	290.03	30.71	29.69	<0.88	...	174	0.69	kn	
167	3335.86	3317.0	1715.14	1691.58	29.25	29.09	0.56	>-0.12	0.21	87	0.05	abo
201	3335.87	3320.0	1713.95	1572.67	25.94	25.81	0.05	>1.63	>1.62	699	0.00	lo
358	3335.87	3332.0	1714.35	1091.36	31.54	31.04	0.86	>-1.07	-1.37	70	0.87	
473	3335.87	3340.4	1713.85	754.28	28.67	28.61	0.15	>0.22	>0.93	81	0.02	abl
168	3335.89	3317.3	1707.01	1679.65	30.04	29.61	0.31	>-0.81	>-1.05	119	0.03	ab
181	3335.89	3317.6	1707.72	1669.03	30.67	30.23	0.54	>-0.75	>-0.72	91	0.13	
382	3335.90	3333.6	1705.03	1027.98	31.61	30.73	<1.57	>-1.29	>-1.23	76	0.86	
551	3335.91	3345.7	1702.81	542.80	31.14	30.82	<0.65	...	50	0.93	kn	

Table 2—Continued

ID	HDF5_J22r-60d	x	y	$m_i$	$m_a$	clr-lp	nuv-clr	fuv-clr	$r_h$	s/g	flags	
101	3335.93	3311.9	1695.71	1896.15	30.22	29.65	<0.90	...	...	118	0.01	kn
601	3335.94	3350.3	1691.30	358.51	31.61	30.80	<0.92	...	...	70	0.87	kn
329	3335.96	3324.1	1687.50	1408.15	29.49	29.07	0.06	>-0.38	>-0.26	133	0.00	
690	3335.97	3301.7	1683.06	2302.89	30.01	29.92	<0.21	...	...	69	0.75	kn
12	3335.97	3303.5	1684.54	2232.71	31.11	30.64	<0.50	...	...	61	0.94	kn
49	3335.97	3307.5	1684.47	2072.93	30.31	30.03	0.58	...	...	112	0.12	kn
157	3335.98	3315.6	1680.19	1746.31	29.85	29.05	<0.55	>-0.78	...	204	0.06	bn
142	3335.98	3315.9	1680.62	1736.09	30.08	29.40	0.18	>-0.81	...	117	0.12	abn
569	3335.99	3346.8	1679.00	500.49	31.06	30.97	<0.88	...	...	63	0.95	kn
453	3336.02	3339.0	1670.38	811.30	28.53	28.32	0.28	>0.36	>1.68	109	0.02	a
459	3336.02	3339.6	1668.64	787.15	28.63	28.42	0.58	>0.00	>0.57	183	0.00	
330	3336.04	3330.3	1662.20	1161.28	29.96	29.86	0.65	>-0.02	>0.53	77	0.07	
233	3336.07	3321.5	1654.51	1510.85	30.36	30.17	0.44	>-0.90	>-0.35	67	0.49	
530	3336.07	3343.4	1654.62	633.93	31.35	30.53	<1.61	...	>-0.57	79	0.77	k
428	3336.10	3336.8	1644.75	901.31	28.40	28.25	0.50	>0.90	>1.41	115	0.02	
247	3336.11	3323.0	1643.76	1449.43	30.85	30.37	<1.09	>-0.92	>-0.91	83	0.60	
370	3336.12	3333.2	1641.00	1041.96	30.64	30.04	<0.93	>-0.98	>-0.05	102	0.43	
290	3336.15	3327.3	1629.77	1277.84	31.11	30.74	<0.58	>-0.73	>0.14	75	0.73	
460	3336.15	3339.4	1631.24	797.15	29.71	29.60	0.37	-0.63	>0.89	87	0.01	
408	3336.16	3335.5	1627.40	953.12	31.69	30.68	<1.55	>-1.67	>-0.23	89	0.84	
525	3336.16	3341.7	1628.25	704.89	31.16	30.74	<1.35	...	>-0.51	62	0.94	k
538	3336.16	3344.6	1626.35	586.85	30.85	30.23	<0.99	...	...	73	0.97	kn
612	3336.16	3351.1	1629.19	328.20	28.57	28.46	0.07	...	...	98	0.03	kn
324	3336.17	3330.0	1626.05	1171.79	26.97	26.89	0.11	0.80	>2.27	138	0.03	
60	3336.18	3308.8	1620.60	2018.97	27.15	27.02	0.45	...	...	244	0.01	kn
254	3336.18	3323.4	1620.90	1436.95	30.13	29.69	0.76	>-0.34	>0.70	97	0.20	
100	3336.19	3311.8	1618.88	1900.86	31.93	30.20	<1.61	...	...	144	0.77	kn
416	3336.19	3336.1	1618.91	925.62	30.92	30.82	<1.30	>-0.56	>0.30	59	0.33	
243	3336.21	3322.6	1613.08	1466.61	28.02	27.92	0.66	>1.12	>1.41	107	0.02	
691	3336.22	3302.0	1609.97	2292.63	30.12	29.53	0.92	...	...	105	0.73	kn
150	3336.22	3316.2	1608.99	1723.88	31.19	30.16	1.16	>-0.76	>-1.02	114	0.71	
334	3336.22	3330.5	1609.42	1152.36	30.42	29.39	<0.81	>-1.14	>-0.29	189	0.03	a
385	3336.22	3333.7	1610.49	1022.62	31.31	30.63	<0.88	>-1.30	-0.36	74	0.92	
510	3336.23	3342.4	1608.08	674.19	30.02	29.56	<0.93	...	>0.00	128	0.12	k
134	3336.25	3314.8	1601.43	1780.56	30.18	29.89	<0.59	>-0.98	>-1.24	109	0.02	
256	3336.25	3324.7	1601.85	1384.83	30.42	30.18	0.93	>-0.31	>0.52	75	0.23	
367	3336.25	3332.7	1601.08	1063.49	31.26	31.03	<1.12	>-0.64	>0.20	49	0.84	
528	3336.25	3341.7	1602.53	701.69	29.64	29.37	0.38	...	>0.36	113	0.01	k
237	3336.28	3321.9	1591.87	1494.82	28.99	28.76	-0.69	>0.74	>1.30	82	0.24	
211	3336.30	3319.9	1586.91	1576.16	31.12	30.58	<0.52	>-0.83	>0.27	83	0.94	
230	3336.30	3321.3	1586.32	1519.24	30.52	29.48	0.92	>-1.14	>0.40	175	0.23	
536	3336.31	3344.7	1582.53	585.23	28.59	28.56	-0.09	...	>1.97	165	0.00	afiko
532	3336.32	3344.1	1580.92	607.35	29.43	29.56	<0.37	...	>0.22	108	0.00	ak
25	3336.33	3305.3	1578.82	2160.86	31.73	30.89	<1.28	...	...	66	0.85	kn
270	3336.33	3326.3	1576.68	1321.14	24.79	24.79	0.31	>3.14	>4.08	238	0.03	
517	3336.33	3343.3	1576.24	641.31	27.74	27.16	0.54	...	>1.13	311	0.00	abk
659	3336.35	3354.4	1571.17	196.50	29.77	29.03	0.52	...	...	126	0.72	kn
16	3336.36	3304.6	1569.82	2185.89	30.03	29.24	0.27	...	...	145	0.02	kn
486	3336.36	3341.0	1569.82	731.33	30.02	29.38	0.76	...	>-0.03	130	0.13	k
176	3336.38	3317.9	1563.44	1656.37	26.53	26.42	0.58	1.55	2.02	202	0.03	b
518	3336.38	3343.5	1563.97	631.17	27.72	27.39	0.52	...	>0.71	233	0.03	abk
373	3336.39	3333.7	1559.26	1022.90	29.85	29.40	0.59	>0.05	>0.83	128	0.12	ab

Table 2—Continued

ID	HDFS_J22r-60d	x	y	$m_i$	$m_a$	clr-lp	nuv-clr	fuv-clr	$r_h$	s/g	flags	
389	3336.39	3334.0	1558.95	1010.61	31.23	30.71	<0.79	>-0.77	>-0.45	69	0.92	a
27	3336.40	3305.5	1557.43	2150.33	30.11	29.75	<0.53	...	...	119	0.66	kn
289	3336.41	3327.3	1554.92	1277.73	29.99	29.94	<0.03	0.08	>0.91	60	0.77	
396	3336.41	3333.4	1554.56	1033.82	29.65	29.46	<0.69	>-0.14	>0.73	116	0.00	b
534	3336.41	3344.1	1554.46	606.77	30.72	30.21	<0.63	...	>-0.74	80	0.04	k
10	3336.44	3302.8	1546.57	2259.61	30.08	29.25	<0.54	...	...	145	0.68	kn
177	3336.44	3317.8	1545.96	1659.35	28.79	28.45	0.26	>0.80	>1.37	107	0.01	ab
205	3336.44	3319.3	1545.92	1599.82	31.16	31.22	<0.88	>-0.96	>-0.05	56	0.88	
590	3336.44	3349.7	1545.80	383.97	30.66	30.26	0.77	...	...	85	0.87	kn
26	3336.48	3305.5	1534.95	2152.75	30.23	29.76	<0.43	...	...	92	0.76	kn
282	3336.53	3326.7	1520.08	1301.56	29.88	29.71	0.27	>-0.31	>0.75	92	0.08	
645	3336.53	3353.3	1518.65	241.02	25.75	25.74	0.39	...	...	159	0.04	kn
438	3336.54	3337.5	1514.73	873.00	28.99	28.91	0.12	>0.65	>1.47	91	0.02	
444	3336.57	3338.3	1505.68	840.74	26.79	26.69	0.25	>1.31	2.68	237	0.03	
622	3336.57	3351.9	1506.84	295.35	30.46	30.09	<0.94	...	...	82	0.96	kn
271	3336.58	3325.7	1502.91	1343.95	28.66	28.64	0.42	>0.88	>1.63	105	0.02	
404	3336.58	3335.2	1504.80	962.79	30.57	30.48	<0.96	>-0.39	>-0.35	101	0.73	fi
116	3336.60	3313.6	1497.55	1827.81	28.43	28.30	0.54	>-1.98	...	179	0.00	ln
376	3336.61	3324.8	1496.31	1380.10	27.66	27.60	0.22	>1.33	>2.38	115	0.03	
524	3336.61	3343.3	1495.43	640.79	29.42	29.33	0.11	...	>0.57	100	0.01	k
597	3336.62	3350.2	1493.57	364.15	27.73	27.69	0.70	...	...	152	0.03	kn
667	3336.62	3354.7	1492.56	182.39	30.38	30.04	<0.77	...	...	76	0.97	bkn
670	3336.65	3355.1	1482.69	165.62	29.92	29.63	0.47	...	...	96	0.85	aehkn
58	3336.66	3308.7	1480.82	2023.96	25.17	25.13	0.24	...	...	409	0.02	kn
309	3336.67	3328.7	1478.84	1222.44	29.80	29.47	0.72	>-0.13	>0.79	108	0.01	
630	3336.69	3352.7	1472.29	264.45	28.95	28.10	0.44	...	...	274	0.01	kn
545	3336.70	3345.4	1469.15	555.36	31.47	30.47	<1.54	...	...	96	0.86	kn
664	3336.70	3354.6	1467.25	186.26	30.00	28.70	<0.33	...	...	177	0.60	kn
9	3336.71	3303.4	1466.92	2233.90	25.89	25.84	0.47	...	...	198	0.03	kn
326	3336.73	3330.0	1459.98	1171.57	29.97	29.54	0.28	>0.01	>0.39	111	0.01	
583	3336.73	3349.2	1460.44	404.18	27.21	27.16	0.00	...	...	127	0.03	abkn
442	3336.74	3337.8	1457.47	860.58	31.22	30.75	<0.82	-0.82	>0.06	74	0.87	
584	3336.74	3349.6	1456.79	386.52	27.59	27.49	0.35	...	...	141	0.03	abkn
238	3336.75	3321.8	1453.36	1499.22	32.05	30.66	<1.26	>-1.14	>-0.38	88	0.72	fi
348	3336.75	3324.1	1452.97	1408.30	30.47	30.30	<0.85	>-0.18	>0.12	69	0.71	
204	3336.76	3319.3	1450.99	1598.76	30.17	29.79	<0.82	>0.00	>0.52	92	0.10	
559	3336.78	3346.1	1446.27	527.94	30.51	30.36	0.48	...	...	58	0.63	kn
567	3336.78	3346.8	1446.03	498.77	29.36	29.20	0.37	...	...	90	0.01	abkn
673	3336.80	3355.3	1439.18	159.39	30.13	...	0.79	...	...	...	0.84	abhkn
568	3336.81	3346.9	1435.98	496.62	29.02	28.78	-0.00	...	...	103	0.01	abkn
668	3336.81	3355.0	1436.58	172.68	29.01	29.78	0.48	...	...	81	0.01	abhkn
663	3336.82	3354.7	1432.72	184.82	29.22	27.32	-0.35	...	...	373	0.01	akn
133	3336.83	3314.4	1431.62	1796.90	29.40	29.29	-0.02	>-1.44	>-0.24	104	0.01	o
431	3336.83	3336.9	1431.19	895.67	28.78	28.54	0.12	>0.11	>1.30	108	0.02	
541	3336.83	3345.2	1430.27	561.62	31.36	30.49	<1.05	...	...	88	0.72	kn
331	3336.84	3330.2	1428.73	1162.93	31.38	30.79	<0.89	>-0.88	>-0.15	79	0.59	
642	3336.86	3353.0	1421.19	252.49	31.22	30.69	<0.93	...	...	52	0.94	kn
117	3336.87	3313.4	1418.90	1833.58	28.89	28.86	0.75	...	...	81	0.02	kn
495	3336.87	3341.9	1418.91	693.61	24.87	24.84	0.18	>5.45	>3.86	195	0.03	abl
657	3336.87	3354.2	1417.70	204.46	30.45	28.96	<0.13	...	...	155	0.98	kn
665	3336.88	3354.7	1416.46	181.84	29.92	28.11	<0.52	...	...	249	0.54	akn
445	3336.89	3337.9	1411.11	857.24	31.28	30.27	<1.01	>-0.79	-0.02	119	0.56	

Table 2—Continued

ID	HDFS_J22r-60d	x	y	$m_i$	$m_a$	clr-lp	nuv-clr	fuv-clr	$r_h$	s/g	flags
466	3336.89	3339.7	1411.73	781.81	30.18	29.96	<0.57	>-0.62	>0.61	76	0.15
616	3336.89	3351.3	1411.65	318.13	29.86	29.70	0.16	...	...	98	0.32
675	3336.89	3355.6	1411.84	146.41	30.72	32.47	<0.95	...	...	25	0.98
485	3336.90	3341.3	1411.05	720.91	30.55	29.89	<0.92	>-1.87	>0.34	106	0.13
496	3336.91	3342.9	1406.27	655.60	22.79	22.79	0.23	>6.59	>3.80	267	0.03
152	3336.92	3316.3	1404.02	1718.89	30.54	30.42	<0.65	>-0.32	>-1.14	55	0.76
484	3336.92	3341.0	1404.07	731.85	29.17	28.87	-0.08	>-0.82	>0.78	101	0.03
78	3336.94	3310.4	1397.10	1955.40	27.80	27.74	0.45	...	...	95	0.02
379	3336.94	3333.5	1397.56	1029.79	31.99	31.26	<1.35	>-1.27	>-0.57	60	0.84
225	3336.95	3320.8	1395.27	1539.40	30.05	29.79	0.52	>-0.11	>0.46	96	0.09
432	3336.96	3336.9	1392.34	896.55	29.88	29.65	<0.22	>-0.20	>0.83	114	0.00
95	3336.98	3311.7	1385.69	1902.29	29.77	29.63	0.30	...	...	73	0.12
155	3336.99	3316.4	1383.03	1715.84	30.85	30.32	0.47	>-0.89	-0.93	76	0.83
216	3336.99	3320.1	1384.06	1566.08	28.79	28.67	0.59	>0.84	>1.60	115	0.01
10123	3336.99	3333.0	1384.14	1052.53	29.21	27.94	-0.24	>0.92	>1.71	138	0.00
628	3337.01	3352.4	1377.37	275.48	30.18	28.87	<0.37	...	...	216	0.66
686	3337.01	3356.6	1376.68	107.11	29.38	27.48	<0.51	...	...	158	0.96
339	3337.02	3330.9	1374.67	1135.01	30.36	30.13	<0.92	>-0.15	>0.45	78	0.18
259	3337.03	3324.7	1372.02	1381.92	31.43	30.86	<1.54	>-0.85	>-0.29	77	0.52
10120	3337.03	3332.5	1371.47	1073.39	28.80	27.15	-0.24	>1.18	>1.81	228	0.00
377	3337.04	3333.6	1367.36	1029.05	31.24	30.98	<1.02	>-0.91	>-0.25	69	0.30
32	3337.05	3306.2	1364.03	2124.64	29.27	29.16	0.58	...	...	92	0.01
160	3337.08	3316.8	1357.51	1700.39	28.40	28.24	-0.26	>0.51	>0.77	130	0.03
300	3337.08	3328.7	1357.69	1223.56	22.58	22.62	0.80	>5.14	>5.73	69	0.96
175	3337.09	3317.5	1353.75	1673.37	30.57	29.61	0.92	>-0.82	>0.12	147	0.18
587	3337.09	3349.7	1353.24	384.76	27.26	27.22	-0.19	...	...	163	0.03
661	3337.10	3353.3	1351.61	240.76	29.93	29.72	<0.02	...	...	77	0.08
226	3337.11	3320.9	1346.30	1536.36	30.63	30.29	<1.16	>-0.62	>-0.06	95	0.64
10121	3337.11	3332.6	1347.46	1066.91	26.65	26.03	0.19	0.67	2.42	251	0.00
102	3337.12	3312.4	1343.86	1876.39	27.39	27.30	0.34	...	...	162	0.03
131	3337.17	3314.3	1329.54	1799.17	29.37	29.11	0.85	>-0.80	>-1.02	100	0.01
91	3337.18	3310.3	1325.60	1960.39	24.91	24.89	0.39	...	...	420	0.03
212	3337.19	3319.9	1324.57	1575.35	31.18	29.77	<1.41	-0.82	>0.09	161	0.79
10100	3337.19	3325.5	1323.08	1351.80	27.98	26.69	0.63	>1.32	>2.19	297	0.00
374	3337.19	3333.4	1324.15	1035.28	31.34	31.06	<1.45	>-0.80	>-0.70	67	0.89
592	3337.22	3349.8	1315.43	381.24	30.30	29.64	0.45	...	...	107	0.74
10119	3337.23	3332.3	1312.78	1077.46	29.35	28.78	0.34	>0.88	>1.68	70	0.04
511	3337.23	3342.5	1312.27	671.04	30.63	30.84	<0.89	...	>-0.14	72	0.89
38	3337.24	3306.3	1309.08	2119.19	29.70	29.53	<0.31	...	...	92	0.03
65	3337.24	3308.8	1308.07	2019.25	30.89	29.59	<1.06	...	...	180	0.14
261	3337.24	3324.9	1309.02	1374.83	29.18	28.83	0.47	>0.79	>0.53	95	0.25
433	3337.24	3336.9	1309.03	895.09	30.72	29.72	<0.74	>-0.40	>0.02	162	0.17
28	3337.26	3305.6	1304.81	2148.89	30.14	29.86	<0.38	...	...	87	0.08
500	3337.27	3341.5	1300.04	710.33	29.07	28.74	<0.41	>-1.28	>0.90	163	0.00
262	3337.28	3325.2	1298.56	1365.20	29.67	29.32	0.72	>0.02	>0.54	122	0.01
462	3337.28	3339.6	1297.19	789.20	30.32	29.72	<0.68	>-0.93	>0.54	124	0.03
169	3337.32	3317.0	1285.98	1689.73	29.97	29.10	0.68	>0.02	>-0.08	199	0.01
222	3337.33	3320.2	1282.27	1564.49	26.00	26.00	0.41	>2.65	>3.29	146	0.03
180	3337.34	3317.5	1278.89	1670.58	30.90	30.13	<0.58	>-0.57	>0.04	142	0.81
467	3337.34	3340.3	1279.99	759.57	25.35	25.36	0.21	>1.63	>4.02	111	0.03
98	3337.37	3311.8	1271.82	1898.75	29.19	29.20	-0.00	...	...	73	0.01
186	3337.39	3317.9	1264.37	1656.14	28.28	28.21	0.50	>1.32	1.31	88	0.02

Table 2—Continued

ID	HDF5_J22r-60d	x	y	$m_i$	$m_a$	clr-lp	nuv-clr	fuv-clr	$r_h$	s/g	flags
413	3337.39	3335.9	1264.59	933.94	30.24	30.26	<0.54	>-0.12	>0.45	79	0.18
231	3337.40	3321.6	1262.78	1505.60	25.36	25.37	0.14	2.01	>3.49	109	0.06
393	3337.40	3334.7	1263.62	984.31	28.37	28.27	0.40	>1.15	>1.62	87	0.05
46	3337.43	3307.1	1252.79	2087.90	30.00	29.77	<0.47	...	...	101	0.07 kn
24	3337.44	3305.3	1250.18	2157.66	28.15	28.10	0.31	...	...	87	0.02 kn
555	3337.44	3345.9	1248.95	534.12	31.55	31.17	<1.12	...	...	43	0.86 kn
580	3337.44	3348.7	1251.15	423.90	30.73	30.01	<0.90	...	...	101	0.70 kn
48	3337.50	3307.4	1232.24	2074.60	29.26	29.00	0.17	...	...	107	0.01 kn
482	3337.50	3340.9	1232.48	734.35	28.05	28.04	-0.32	0.65	>1.59	115	0.02
519	3337.51	3342.8	1229.87	657.98	29.80	29.63	<0.43	...	-0.25	72	0.13 k
602	3337.52	3350.4	1225.46	355.92	30.79	30.23	<1.10	...	...	82	0.91 kn
40	3337.58	3306.5	1210.51	2111.76	31.21	29.68	<1.42	...	...	187	0.91 kn
141	3337.58	3315.7	1209.18	1742.61	26.00	25.96	0.36	0.77	>1.75	204	0.03
10103	3337.59	3329.1	1205.73	1206.06	17.78	17.83	0.34	1.77	2.53	188	0.85 cfgijmpq
607	3337.60	3350.9	1202.68	337.39	28.13	27.97	0.44	...	...	137	0.02 kn
1	3337.60	3355.3	1204.05	161.27	17.14	17.16	0.79	...	...	274	0.85 acefhikn
51	3337.62	3307.6	1196.36	2068.34	29.72	29.70	0.49	...	...	64	0.19 kn
588	3337.62	3349.9	1198.57	376.67	26.31	26.25	0.56	...	...	229	0.03 kn
179	3337.64	3318.0	1190.31	1652.84	26.05	25.98	0.22	1.89	>2.07	321	0.03 a
456	3337.68	3339.0	1178.40	810.44	29.59	29.17	<0.19	>-0.15	>0.86	155	0.01
469	3337.68	3340.0	1179.28	770.44	30.16	29.81	<0.51	>-0.67	>0.32	78	0.06
273	3337.71	3325.9	1171.99	1337.34	29.10	28.88	0.17	>0.64	>0.57	139	0.01 a
639	3337.71	3347.7	1170.28	462.49	31.95	31.09	<2.00	...	...	62	0.81 kn
103	3337.72	3312.3	1167.35	1880.72	30.18	30.15	<0.34	...	...	68	0.19 kn
236	3337.73	3321.8	1164.70	1500.23	30.02	28.92	<0.93	>-0.12	>0.09	235	0.13
423	3337.73	3336.4	1165.86	916.07	29.88	29.48	<0.37	>-0.07	>0.55	126	0.00
130	3337.75	3314.2	1157.76	1803.03	30.65	29.89	<1.18	...	...	153	0.96 kn
7	3337.77	3302.3	1153.69	2279.29	27.41	27.13	0.30	...	...	147	0.03 aehkn
417	3337.79	3336.2	1146.51	923.23	30.53	29.98	<1.10	>-0.47	>0.27	97	0.63
173	3337.81	3317.7	1140.67	1665.26	25.68	25.66	0.40	0.78	>2.67	187	0.03
253	3337.81	3324.4	1142.48	1394.05	22.85	22.84	0.48	0.89	1.86	553	0.03 a
403	3337.83	3335.2	1136.64	962.58	28.84	28.81	-0.00	>0.41	>1.06	68	0.07
52	3337.86	3307.6	1125.02	2067.53	30.89	29.38	0.75	...	...	208	0.52 kn
573	3337.86	3347.0	1126.62	489.92	31.58	30.97	<0.93	...	...	66	0.84 kn
493	3337.87	3341.3	1122.37	718.20	31.75	31.32	<1.08	>-2.15	>-0.14	55	0.73
512	3337.88	3342.6	1119.29	669.06	29.03	28.92	0.33	...	>1.05	66	0.46 k
383	3337.90	3334.1	1115.72	1006.97	26.18	26.17	0.23	1.80	>2.31	167	0.03
548	3337.91	3345.7	1111.09	543.58	29.91	29.52	<0.92	...	...	148	0.00 kn
19	3337.92	3304.8	1107.90	2178.81	28.67	28.56	0.31	...	...	93	0.01 kn
543	3337.93	3345.3	1106.44	557.65	30.59	29.71	<0.41	...	>-0.86	168	0.95 ako
497	3337.95	3341.7	1101.35	701.55	30.73	30.19	0.87	>-1.38	>0.17	75	0.91
146	3337.98	3314.6	1092.48	1786.73	26.48	26.36	0.69	>0.73	>1.39	465	0.00 lo
483	3337.99	3340.9	1088.85	736.59	31.57	31.04	<1.07	>-1.48	>-0.34	64	0.84
89	3338.00	3311.8	1083.88	1900.90	27.89	27.86	-0.12	...	...	196	0.03 kn
126	3338.00	3313.6	1085.19	1826.33	30.86	30.00	<0.72	...	...	122	0.47 akn
457	3338.01	3339.4	1082.25	797.05	27.95	27.77	-0.20	1.11	>1.53	123	0.03 ab
272	3338.02	3325.7	1077.92	1345.30	29.07	28.89	-0.27	>0.60	>0.58	118	0.01
344	3338.02	3331.2	1078.20	1125.29	31.35	30.82	<1.14	>-0.81	>-0.45	72	0.81 a
47	3338.04	3307.0	1073.68	2090.40	30.79	29.56	<1.04	...	...	181	0.58 kn
135	3338.04	3313.8	1073.69	1820.19	30.63	30.05	<0.96	...	...	115	0.21 akn
235	3338.05	3321.6	1070.58	1508.27	31.52	30.89	<0.82	>-0.95	>-0.73	62	0.86
269	3338.06	3325.4	1068.91	1355.69	31.03	30.15	<0.93	>-0.46	>-0.23	135	0.89 a

Table 2—Continued

ID	HDFS-J22r-60d	x	y	$m_i$	$m_a$	clr-lp	nuv-clr	fuv-clr	$r_h$	s/g	flags	
575	3338.06	3347.1	1066.68	485.60	29.68	29.29	<0.28	...	154	0.01	kn	
8	3338.07	3302.6	1065.55	2267.19	26.11	25.86	0.59	...	341	0.03	aehkn	
132	3338.07	3314.3	1065.57	1800.68	31.70	32.00	<1.07	...	42	0.87	kn	
50	3338.08	3308.4	1062.58	2035.87	24.03	23.99	0.45	...	566	0.03	bkn	
458	3338.08	3339.5	1060.67	791.19	27.25	27.05	0.04	1.01	>2.33	275	0.01	ab
11	3338.10	3303.4	1054.64	2233.59	30.65	30.00	0.41	...	77	0.97	kn	
221	3338.11	3320.5	1053.91	1551.57	30.34	30.08	<0.29	>-0.56	>0.34	82	0.04	
354	3338.11	3324.4	1053.36	1393.63	29.04	29.04	0.15	>0.62	>0.99	96	0.01	
77	3338.14	3310.0	1044.17	1970.11	24.94	24.93	0.21	...	215	0.03	abkn	
111	3338.14	3312.9	1043.80	1856.05	30.78	30.58	<0.86	...	83	0.10	kn	
203	3338.14	3319.4	1044.18	1595.08	27.59	27.48	0.21	0.56	>1.42	200	0.02	
535	3338.14	3344.5	1043.29	592.01	29.29	29.07	0.13	...	0.31	153	0.00	k
646	3338.15	3353.5	1040.86	232.87	29.88	29.02	<0.10	...	181	0.02	akn	
631	3338.17	3352.6	1035.05	268.60	31.03	31.14	<1.23	...	48	0.74	kn	
465	3338.18	3339.3	1030.87	797.70	29.19	28.94	0.24	>0.33	>1.00	140	0.00	a
123	3338.19	3313.7	1027.88	1824.38	28.58	28.21	-0.32	...	209	0.00	kn	
307	3338.19	3328.7	1030.23	1221.62	29.34	28.66	0.46	>0.34	>0.58	162	0.00	
369	3338.20	3333.2	1025.41	1042.94	30.11	29.91	1.04	>0.05	>0.41	68	0.23	
266	3338.21	3325.3	1024.59	1357.52	30.54	30.05	<0.46	>-0.65	>0.02	104	0.14	abfi
353	3338.21	3331.9	1023.14	1094.84	28.77	28.72	0.52	>0.43	>0.78	80	0.19	
147	3338.23	3316.3	1017.34	1719.35	27.52	27.44	0.35	1.31	>1.20	119	0.06	
232	3338.23	3321.4	1018.00	1514.52	27.35	27.29	0.47	>1.75	>2.22	151	0.03	
333	3338.23	3330.4	1016.84	1154.10	30.22	29.30	0.70	>-0.13	>0.18	164	0.04	
20	3338.24	3304.8	1014.60	2179.79	30.71	30.13	<0.75	...	71	0.97	kn	
301	3338.24	3323.7	1015.11	1422.88	31.55	30.94	<1.09	>-0.82	>-0.44	58	0.85	
371	3338.24	3333.3	1015.04	1039.74	31.12	30.12	<1.60	>-0.70	>-0.35	108	0.93	a
164	3338.25	3317.2	1010.81	1683.34	29.95	29.50	<0.71	>-0.80	>-0.66	103	0.19	ab
653	3338.25	3353.8	1011.08	219.04	29.97	30.08	<0.02	...	69	0.78	kn	
163	3338.26	3317.0	1009.62	1692.95	30.30	29.26	0.37	>-0.47	>-0.73	165	0.11	ab
165	3338.26	3317.4	1007.70	1674.55	29.78	29.44	0.24	>0.18	>-0.28	100	0.03	ab
347	3338.27	3331.5	1004.42	1109.49	29.87	29.61	0.14	>-0.49	>0.21	97	0.00	
494	3338.27	3341.4	1006.29	716.28	30.06	29.78	<0.05	>-0.60	>0.26	84	0.23	
224	3338.28	3320.7	1002.07	1542.24	30.46	29.74	<1.05	>-0.30	>0.19	126	0.10	
352	3338.30	3324.7	996.84	1382.40	29.65	28.77	0.49	>-0.15	>0.47	229	0.01	abfi
678	3338.33	3355.7	988.82	142.13	29.21	28.18	0.40	...	211	0.02	akn	
499	3338.34	3341.9	983.88	695.85	28.31	28.28	0.28	>0.02	1.12	86	0.03	
682	3338.34	3356.2	985.63	121.93	28.83	...	0.69	...	...	0.02	ahkn	
684	3338.36	3356.6	979.46	107.72	28.96	26.56	0.42	...	610	0.01	aehkn	
79	3338.37	3310.7	975.35	1941.55	26.73	26.64	0.12	...	192	0.03	bkn	
2	3338.37	3357.2	976.59	81.48	28.43	25.50	<1.85	...	1004	0.01	aehkn	
506	3338.39	3342.3	971.48	678.64	30.27	29.85	0.62	>-0.74	>0.05	88	0.22	l
195	3338.41	3318.8	965.31	1618.55	28.55	27.94	0.49	>0.75	>1.13	276	0.00	b
263	3338.41	3325.0	964.34	1370.61	31.10	30.56	<0.78	>-1.26	>-0.39	98	0.82	
5	3338.41	3357.4	965.10	76.01	29.96	27.16	<1.08	...	382	0.90	adehkn	
196	3338.42	3319.2	961.53	1604.55	30.04	29.52	0.52	>-0.12	>0.25	120	0.00	ab
279	3338.42	3326.4	960.27	1317.40	30.95	30.62	0.83	>-0.58	>-0.17	68	0.89	
452	3338.42	3338.6	961.44	825.72	29.61	29.49	0.51	0.26	>0.92	73	0.09	
80	3338.43	3310.8	958.11	1937.99	28.72	28.68	-0.64	...	76	0.02	abkn	
687	3338.43	3356.8	957.39	98.48	30.29	28.09	<1.12	...	257	0.98	ehkn	
605	3338.44	3351.1	956.25	326.08	26.45	26.40	0.38	...	216	0.03	akn	
685	3338.44	3356.5	956.49	112.84	30.50	...	0.51	...	...	0.93	hkn	
660	3338.45	3354.4	951.39	194.64	30.88	30.00	1.01	...	104	0.83	kn	

Table 2—Continued

ID	HDF5_J22r-60d	x	y	$m_i$	$m_a$	clr-lp	nuv-clr	fuv-clr	$r_h$	s/g	flags
161	3338.47	3316.8	947.06	1697.76	29.43	29.02	-0.16	>-0.76	>-0.24	123	0.01
681	3338.47	3355.9	947.45	137.27	30.78	29.32	<0.37	...	...	164	0.98
10097	3338.48	3324.0	944.86	1411.95	30.02	29.04	0.11	>0.26	>0.87	75	0.80
128	3338.49	3314.2	940.74	1804.13	28.61	28.37	0.08	...	...	115	0.02
68	3338.50	3309.6	938.16	1988.42	31.15	30.75	<1.28	...	...	63	0.88
99	3338.50	3311.8	938.23	1897.62	29.55	29.05	0.51	...	...	154	0.04
53	3338.51	3307.6	934.03	2066.79	30.42	29.72	<0.99	...	...	117	0.34
656	3338.51	3353.2	933.84	244.10	29.92	29.25	0.66	...	...	137	0.20
6	3338.51	3357.5	934.69	69.53	27.68	26.29	<-0.27	...	...	287	0.04
129	3338.53	3314.5	928.29	1793.00	27.34	27.16	0.08	...	...	197	0.03
514	3338.55	3342.5	922.92	671.21	30.34	29.85	0.81	...	>0.36	98	0.20
411	3338.56	3335.7	919.41	943.77	31.26	30.48	<1.58	>-0.87	>-0.40	82	0.90
529	3338.60	3344.3	909.40	600.07	24.75	24.73	0.35	...	>0.97	296	0.03
662	3338.60	3354.5	909.61	190.59	29.74	29.33	<0.53	...	...	94	0.10
36	3338.63	3306.5	899.28	2109.88	27.82	27.70	0.18	...	...	156	0.03
182	3338.63	3317.6	900.26	1669.16	31.12	30.69	<1.25	>-0.87	>-1.39	71	0.90
599	3338.63	3350.1	898.17	368.97	29.06	28.98	0.14	...	...	83	0.02
654	3338.63	3353.8	898.31	219.64	31.23	30.69	<0.71	...	...	76	0.87
515	3338.64	3342.7	897.84	661.59	30.57	30.24	0.84	...	>-0.21	88	0.39
395	3338.65	3334.8	894.14	980.68	27.79	27.77	0.04	1.63	>1.58	79	0.07
37	3338.66	3306.8	890.33	2099.85	28.96	28.83	0.31	...	...	95	0.01
178	3338.67	3317.5	888.57	1671.46	30.52	30.12	0.72	>-0.56	>-0.82	97	0.13
669	3338.67	3348.3	887.25	437.76	31.69	30.55	<1.16	...	...	98	0.78
145	3338.68	3315.9	883.27	1737.12	31.63	30.44	0.99	>-1.13	>-1.27	109	0.84
4	3338.68	3357.4	885.05	75.76	29.07	28.79	<0.66	...	...	96	0.02
96	3338.69	3311.9	880.31	1896.85	27.62	27.58	0.16	...	...	157	0.03
10173	3338.70	3349.5	879.48	392.73	29.65	28.17	0.71	...	...	133	0.00
119	3338.75	3313.7	864.69	1822.33	30.05	29.85	<0.49	...	...	89	0.08
394	3338.76	3334.7	860.24	984.43	28.98	28.90	0.65	>0.75	>1.16	90	0.01
648	3338.76	3348.3	861.34	438.66	30.46	29.27	<1.18	...	...	195	0.11
207	3338.77	3319.9	858.45	1575.85	25.22	25.20	0.49	>2.89	>3.02	284	0.03
306	3338.77	3328.6	857.58	1226.35	29.59	29.56	<0.41	>0.33	>0.62	83	0.01
45	3338.78	3307.6	855.48	2068.22	25.69	25.65	0.57	...	...	212	0.03
174	3338.79	3317.4	851.49	1675.68	29.23	29.20	0.13	>0.45	>0.07	76	0.12
641	3338.79	3347.9	851.45	456.67	31.45	29.58	1.06	...	...	193	0.87
349	3338.82	3331.9	844.17	1097.26	27.21	27.16	0.17	0.47	1.58	239	0.02
90	3338.83	3311.6	841.70	1908.16	30.76	30.79	0.90	...	...	40	0.97
533	3338.83	3344.1	839.92	607.89	28.72	28.67	-0.22	...	>0.47	61	0.85
138	3338.84	3315.0	836.56	1772.30	31.14	30.52	<1.46	...	...	73	0.93
424	3338.84	3337.2	836.60	882.61	25.25	25.20	0.27	1.52	>3.30	359	0.03
562	3338.86	3346.4	831.81	517.32	30.21	30.09	<0.72	...	...	63	0.44
550	3338.87	3345.7	829.29	542.75	32.01	31.16	<1.26	...	>-2.06	71	0.78
593	3338.87	3349.9	828.05	374.32	26.46	26.45	0.07	...	...	102	0.03
64	3338.89	3310.1	823.04	1968.47	23.68	23.65	0.45	...	...	544	0.03
478	3338.91	3340.6	815.88	748.79	30.83	29.86	<1.24	...	>0.10	158	0.11
619	3338.91	3347.4	817.38	473.57	30.63	30.43	<1.19	...	...	139	0.86
363	3338.94	3332.6	806.89	1067.48	29.01	28.50	0.46	>-0.25	>0.85	181	0.01
563	3338.94	3346.5	807.81	512.45	29.99	29.36	0.25	...	...	139	0.01
481	3338.95	3340.7	805.97	741.56	31.15	30.05	<1.41	...	>-0.46	160	0.80
33	3338.97	3304.2	798.19	2203.79	30.05	29.73	<0.28	...	...	59	0.97
629	3339.00	3347.7	790.07	464.36	30.88	30.56	<1.15	...	...	77	0.90
581	3339.00	3348.7	788.96	421.97	30.47	30.23	<0.91	...	...	75	0.34

Table 2—Continued

ID	HDFS_J22r-60d	x	y	$m_i$	$m_a$	clr-lp	nuv-clr	fuv-clr	$r_h$	s/g	flags	
121	3339.01	3313.8	788.74	1819.80	29.79	29.65	<0.30	...	...	69	0.28	kn
356	3339.01	3332.2	788.74	1081.48	28.82	28.29	0.80	>-0.09	>0.25	227	0.00	
410	3339.01	3335.7	786.52	942.93	30.40	29.83	0.49	>-1.25	>0.02	108	0.01	
292	3339.03	3327.5	782.57	1269.76	31.56	30.80	<1.00	>-0.97	>-0.68	71	0.76	
343	3339.03	3331.2	781.93	1124.79	28.79	28.65	0.63	>0.52	>1.07	93	0.02	
632	3339.03	3352.5	782.90	270.34	31.51	31.31	<0.83	...	...	57	0.90	kn
666	3339.05	3354.7	774.46	185.12	31.05	30.79	<0.65	...	...	66	0.94	kn
31	3339.06	3306.2	771.22	2122.41	25.33	25.31	0.69	...	...	175	0.03	kn
436	3339.06	3337.2	773.22	884.12	30.47	30.34	<0.91	>-0.67	>0.33	67	0.14	
214	3339.09	3320.1	763.34	1566.80	30.44	29.83	<0.63	>-0.86	>-0.15	148	0.94	ab
148	3339.10	3316.2	761.05	1722.30	28.69	28.60	0.37	0.56	>-0.14	74	0.55	
299	3339.11	3323.6	757.17	1426.22	31.25	30.82	<1.18	>-1.09	>-0.43	66	0.90	
258	3339.11	3325.0	758.66	1372.64	28.19	27.78	0.16	>0.27	>1.15	277	0.00	
314	3339.11	3329.0	758.29	1209.82	30.82	30.38	<0.57	>-1.22	>-0.45	102	0.95	b
549	3339.13	3345.6	752.21	547.19	31.42	29.88	<0.94	...	>-0.64	157	0.90	k
633	3339.13	3347.9	751.54	454.26	27.20	27.18	0.58	...	...	130	0.03	kn
676	3339.14	3355.7	749.43	141.60	26.96	26.91	0.23	...	...	96	0.03	kn
209	3339.15	3320.9	747.39	1536.73	27.03	26.98	0.20	0.46	>2.05	170	0.03	ab
42	3339.16	3303.9	741.58	2216.66	29.88	29.72	0.66	...	...	72	0.23	ehkn
208	3339.16	3320.2	744.27	1564.31	28.11	27.79	0.17	>0.60	1.37	196	0.02	ab
125	3339.19	3314.3	733.72	1797.47	25.82	25.78	0.09	...	...	267	0.03	kn
405	3339.19	3335.3	732.98	958.53	31.45	30.96	1.22	>-1.28	>-1.04	55	0.88	
360	3339.20	3332.2	730.66	1085.23	31.64	30.32	<1.31	>-1.39	>-1.29	143	0.86	
351	3339.21	3331.7	728.15	1101.85	30.40	30.18	<0.66	>-0.99	>-0.90	71	0.14	
539	3339.21	3345.1	728.01	566.21	30.79	30.17	0.68	...	>-2.25	85	0.95	ko
56	3339.22	3304.1	723.98	2207.54	29.89	29.55	0.46	...	...	92	0.52	kn
384	3339.23	3324.4	723.28	1396.72	31.31	30.70	0.95	>-1.05	-0.42	67	0.91	
471	3339.23	3340.1	722.34	766.96	30.91	30.48	<0.75	>-1.04	>0.15	104	0.88	
614	3339.23	3350.0	723.62	372.01	30.96	30.67	<0.67	...	...	74	0.19	kn
62	3339.24	3308.5	718.09	2030.21	28.53	28.41	-0.02	...	...	86	0.10	kn
679	3339.26	3355.9	713.49	137.22	27.98	27.87	0.42	...	...	101	0.03	abkn
390	3339.28	3334.1	707.45	1008.86	30.87	30.60	<0.68	>-0.91	>0.21	58	0.94	
30	3339.29	3306.7	705.88	2102.39	26.55	26.46	0.47	...	...	147	0.03	abkn
463	3339.30	3339.5	702.65	789.86	29.79	29.86	0.03	>-0.67	-0.88	56	0.25	
680	3339.31	3356.0	699.02	132.96	27.08	26.98	0.50	...	...	156	0.03	abkn
13	3339.32	3303.4	694.40	2235.75	26.29	26.08	0.77	...	...	261	0.03	aehkn
332	3339.32	3330.3	695.56	1158.14	29.36	29.24	0.23	>0.04	>-0.06	78	0.01	
342	3339.35	3323.1	686.36	1446.03	26.31	26.30	0.09	>2.01	>2.40	86	0.60	ab
359	3339.35	3332.2	687.41	1084.87	30.88	30.09	<1.18	>-1.40	>-0.95	99	0.95	
388	3339.35	3333.9	688.44	1014.05	29.77	29.76	<0.34	>-0.60	>-0.19	55	0.42	
450	3339.35	3338.6	687.77	828.67	27.81	27.77	0.23	>0.45	>0.76	135	0.03	
29	3339.36	3306.2	684.68	2122.86	24.94	24.76	0.43	...	...	488	0.03	abkn
106	3339.39	3312.6	674.86	1866.37	30.19	29.98	<0.43	...	...	82	0.01	kn
198	3339.41	3318.6	670.76	1625.66	31.06	30.40	<0.96	>-1.06	>-1.19	80	0.58	
624	3339.41	3352.0	670.09	290.57	31.36	30.81	1.57	...	...	72	0.88	kn
323	3339.42	3329.5	667.50	1191.38	29.88	29.74	<0.26	>-0.79	>-1.48	84	0.11	
415	3339.42	3336.2	666.88	924.02	28.71	28.52	-0.47	>-0.50	>-0.17	131	0.01	
328	3339.43	3330.1	662.45	1168.22	31.29	31.03	<0.87	>-2.17	>-2.32	49	0.90	
241	3339.44	3322.8	661.27	1459.97	25.19	25.17	0.37	>1.52	>1.65	318	0.03	b
310	3339.44	3328.7	661.70	1224.06	30.54	30.41	0.55	>-1.87	-2.17	81	0.24	
451	3339.45	3338.6	657.88	828.66	30.94	30.12	<1.14	>-1.97	>-1.22	115	0.92	
81	3339.46	3310.7	654.80	1942.59	27.22	27.20	0.41	...	...	107	0.05	kn

Table 2—Continued

ID	HDFS_J22r-60d	x	y	$m_i$	$m_a$	clr-lp	nuv-clr	fuv-clr	$r_h$	s/g	flags	
108	3339.46	3312.7	653.69	1861.52	29.26	29.11	0.31	...	...	82	0.33	kn
183	3339.46	3318.0	653.60	1650.67	26.86	26.83	0.38	>1.10	1.37	137	0.03	
526	3339.48	3343.4	649.14	634.34	30.98	30.98	<1.00	...	>-1.28	74	0.85	ak
689	3339.48	3357.2	648.67	83.78	30.63	29.71	<0.22	...	...	97	0.97	hkn
114	3339.50	3313.0	641.60	1851.70	31.02	30.14	<0.63	...	...	103	0.87	akn
621	3339.51	3351.7	640.55	301.57	30.96	30.45	<1.21	...	...	77	0.18	kn
220	3339.52	3320.4	637.32	1553.93	30.49	29.64	<1.03	>-1.25	>-0.35	135	0.46	
594	3339.53	3350.1	634.82	366.80	26.72	26.68	0.42	...	...	146	0.03	kn
617	3339.54	3351.3	631.45	319.60	29.95	29.47	<0.71	...	...	112	0.01	kn
107	3339.55	3312.6	627.50	1869.26	31.26	30.65	0.99	...	...	80	0.79	kn
470	3339.55	3340.1	628.32	769.17	30.14	29.82	0.30	>-1.39	>-0.96	81	0.32	
429	3339.56	3336.7	626.47	902.11	28.53	28.50	0.70	>-0.65	>0.41	73	0.78	
320	3339.58	3328.1	618.27	1246.28	30.86	30.20	0.72	>-1.71	>-1.97	83	0.85	
372	3339.58	3333.9	620.10	1013.64	26.88	26.67	0.19	0.19	>0.63	305	0.00	o
127	3339.59	3314.1	617.27	1805.63	29.21	29.01	0.65	...	...	108	0.01	kn
604	3339.60	3350.7	613.83	344.51	28.27	28.04	-0.04	...	...	145	0.02	akn
683	3339.60	3356.2	614.07	122.89	30.35	30.01	<0.84	...	...	67	0.97	kn
158	3339.61	3316.7	611.41	1703.48	28.80	28.49	0.12	>-0.42	...	179	0.00	n
84	3339.62	3310.7	606.95	1944.88	31.16	30.54	<1.07	...	...	96	0.85	kn
440	3339.62	3337.7	607.97	863.34	30.54	30.19	<0.41	>-2.01	>-1.42	92	0.60	lo
296	3339.64	3327.8	601.96	1259.65	30.73	30.47	0.93	>-2.20	>-1.80	74	0.62	
505	3339.66	3342.1	594.44	685.98	31.17	30.35	<1.15	...	...	100	0.87	kn
55	3339.67	3308.5	593.38	2030.70	25.88	25.66	0.33	...	...	275	0.03	abkn
136	3339.68	3314.9	590.55	1776.20	29.68	28.92	0.66	...	...	182	0.02	kn
94	3339.69	3311.8	585.52	1900.10	28.39	28.25	0.20	...	...	152	0.01	kn
674	3339.69	3355.9	587.74	136.97	27.17	26.81	0.65	...	...	249	0.03	kn
634	3339.70	3352.6	583.61	267.95	31.57	30.90	0.91	...	...	65	0.85	kn
215	3339.71	3320.1	579.64	1568.17	30.38	29.87	<0.80	>-1.72	>-1.49	92	0.81	
658	3339.73	3353.2	575.93	244.04	31.28	30.59	<1.28	...	...	83	0.89	kn
54	3339.74	3308.5	571.35	2030.73	24.49	24.38	0.31	...	...	471	0.03	abkn
361	3339.74	3332.2	571.26	1082.31	29.81	29.78	<0.02	...	...	84	0.01	kn
553	3339.75	3345.9	568.06	534.99	31.38	30.77	<1.63	...	...	72	0.81	kn
97	3339.77	3311.7	561.69	1903.07	30.07	29.83	<0.19	...	...	71	0.25	kn
598	3339.77	3350.0	561.94	370.70	29.55	29.36	0.36	...	...	77	0.02	kn
249	3339.78	3323.3	560.88	1439.02	26.04	26.05	0.76	>1.71	>1.97	64	0.99	
516	3339.78	3342.8	559.97	658.98	29.38	29.22	0.79	...	...	72	0.23	kn
197	3339.81	3318.1	551.41	1645.91	27.89	27.79	0.39	>-0.19	...	170	0.02	n
297	3339.82	3327.9	547.46	1254.69	31.55	30.79	<1.39	...	...	82	0.85	kn
308	3339.83	3328.8	546.88	1218.37	27.69	27.69	-0.49	>1.91	>1.96	138	0.03	lo
93	3339.84	3311.7	543.08	1904.25	29.13	29.04	0.26	...	...	88	0.01	kn
357	3339.86	3332.1	536.42	1089.18	30.93	30.04	<1.00	...	...	129	0.59	kn
595	3339.87	3350.0	534.67	371.01	28.95	28.84	0.08	...	...	80	0.03	kn
82	3339.91	3310.6	522.50	1945.41	29.69	29.27	0.28	...	...	115	0.01	kn
304	3339.92	3324.0	520.16	1411.36	27.49	27.49	0.03	...	...	81	0.04	kn
171	3339.93	3317.2	516.79	1684.95	31.49	30.59	<1.45	>-4.11	...	83	0.78	ln
391	3339.95	3334.2	510.86	1003.28	30.66	30.47	0.59	...	...	70	0.84	kn
14	3339.98	3305.1	502.50	2167.46	21.40	21.39	0.73	...	...	739	0.03	aehkn
492	3339.98	3341.2	501.85	722.24	31.13	30.89	<1.26	...	...	55	0.89	kn
402	3339.99	3335.0	497.60	972.47	29.66	29.59	<0.52	...	...	89	0.01	kn
479	3340.00	3340.7	496.46	743.32	31.46	30.78	<1.28	...	...	78	0.88	kn
188	3340.01	3317.9	491.90	1655.27	31.47	31.04	<1.12	...	...	58	0.89	kn
544	3340.01	3345.3	491.62	558.92	31.38	31.01	<1.10	...	...	50	0.88	kn

Table 2—Continued

ID	HDFS_J22r-60d	x	y	$m_i$	$m_a$	clr-lp	nuv-clr	fuv-clr	$r_h$	s/g	flags
513	3340.02	3342.6	488.36	669.05	31.35	30.85	<1.18	...	75	0.91	kn
671	3340.02	3355.2	489.89	162.65	30.98	30.45	<0.42	...	80	0.95	kn
437	3340.04	3337.3	483.26	877.89	30.74	30.17	<0.55	...	98	0.14	kn
246	3340.11	3323.2	463.05	1443.51	27.41	27.39	0.26	...	109	0.03	kn
401	3340.11	3334.9	462.68	976.40	30.22	29.69	<0.42	...	103	0.19	kn
362	3340.12	3332.4	458.77	1076.56	30.46	29.80	1.22	...	122	0.05	kn
144	3340.13	3316.6	458.12	1708.07	25.18	25.20	0.72	...	128	0.93	kn
337	3340.17	3330.8	444.75	1139.28	30.27	29.78	<0.22	...	106	0.08	kn
540	3340.19	3345.3	439.25	560.23	29.41	29.23	0.24	...	106	0.01	kn
582	3340.20	3348.9	437.05	413.71	28.17	27.91	0.13	...	148	0.02	kn
561	3340.21	3346.6	434.70	508.99	26.23	26.18	0.61	...	204	0.03	kn
677	3340.21	3355.8	433.23	139.83	28.87	28.64	0.35	...	151	0.01	kn
609	3340.22	3351.4	430.35	315.36	26.27	26.13	0.04	...	309	0.00	bkn
206	3340.25	3319.5	420.82	1591.13	30.20	29.71	<0.87	...	115	0.09	kn
71	3340.28	3309.9	412.40	1977.10	31.20	31.15	<0.96	...	78	0.82	bkn
586	3340.30	3349.4	405.99	395.08	31.60	31.29	<1.00	...	48	0.86	kn
120	3340.33	3313.7	396.70	1824.45	31.37	31.20	<0.88	...	57	0.93	kn
313	3340.33	3328.9	398.11	1214.14	29.25	29.18	-0.06	...	102	0.01	kn
69	3340.35	3309.8	392.78	1978.63	30.45	29.82	<1.09	...	117	0.14	kn
498	3340.35	3341.8	392.57	698.00	28.78	28.60	0.47	...	107	0.03	kn
608	3340.35	3351.0	392.81	330.66	26.25	26.24	-0.03	...	128	0.03	abkn
191	3340.38	3318.7	384.20	1621.99	25.17	25.15	0.29	...	275	0.03	kn
464	3340.41	3339.8	375.42	779.82	28.63	28.53	0.61	...	156	0.01	kn
520	3340.41	3343.2	373.60	645.20	26.68	26.55	0.28	...	290	0.00	kn
264	3340.42	3325.1	371.80	1365.35	26.93	26.90	0.63	...	102	0.03	kn
380	3340.42	3333.7	370.62	1023.09	27.88	27.68	0.28	...	154	0.03	kn
507	3340.45	3342.3	363.99	680.14	31.55	31.56	<1.13	...	49	0.83	kn
655	3340.45	3354.1	362.39	208.30	26.44	26.43	0.14	...	97	0.03	kn
427	3340.47	3336.7	357.24	904.70	28.30	27.94	0.06	...	205	0.01	kn
124	3340.50	3314.0	348.99	1813.25	31.96	30.91	<1.52	...	73	0.82	kn
501	3340.50	3342.1	347.22	686.32	28.15	27.96	0.02	...	177	0.02	kn
560	3340.50	3346.3	347.43	519.74	28.97	28.75	0.68	...	112	0.01	kn
166	3340.51	3317.0	343.45	1693.28	30.60	30.18	<1.12	...	88	0.19	kn
556	3340.52	3345.9	343.50	534.16	30.97	30.70	<1.16	...	61	0.92	kn
268	3340.53	3325.4	337.57	1356.41	30.23	29.64	<0.90	...	114	0.11	kn
315	3340.53	3329.1	339.90	1206.27	29.41	29.14	-0.02	...	152	0.00	kn
23	3340.57	3305.2	327.26	2164.22	30.15	29.90	0.16	...	67	0.92	kn
336	3340.57	3330.9	326.00	1136.77	28.86	28.79	0.07	...	90	0.01	kn
122	3340.61	3313.8	314.68	1817.92	30.85	30.51	<0.59	...	70	0.57	kn
218	3340.61	3320.1	315.35	1569.14	30.80	30.44	0.44	...	67	0.93	kn
267	3340.61	3325.2	316.73	1363.68	30.77	30.86	<1.02	...	40	0.96	kn
422	3340.61	3336.4	316.40	915.23	30.13	29.87	<0.43	...	106	0.96	bkn
480	3340.63	3340.8	309.03	737.88	28.40	28.12	0.62	...	148	0.02	kn
638	3340.65	3352.7	304.46	262.79	30.98	30.52	<1.23	...	60	0.95	kn
397	3340.66	3334.7	301.88	984.73	29.47	29.33	<0.46	...	102	0.02	kn
589	3340.66	3349.7	300.60	382.94	26.17	26.17	0.67	...	66	0.98	kn
143	3340.67	3315.5	298.02	1749.95	30.09	29.85	<0.69	...	89	0.40	kn
115	3340.69	3313.2	292.94	1843.22	30.20	30.03	<0.68	...	61	0.70	kn
260	3340.69	3324.8	292.40	1380.84	30.07	30.00	<-0.07	...	57	0.38	kn
312	3340.69	3328.7	293.12	1222.92	29.68	29.27	<0.77	...	143	0.01	kn
649	3340.71	3353.4	284.73	234.05	30.88	30.25	<1.33	...	63	0.95	kn
22	3340.72	3305.0	282.41	2172.15	30.80	30.55	<0.88	...	54	0.97	kn

Table 2—Continued

ID	HDFS_J22r-60d	x	y	$m_i$	$m_a$	clr-lp	nuv-clr	fuv-clr	$r_h$	s/g	flags
468	3340.73	3339.6	280.77	788.99	30.11	29.80	<1.00	...	99	0.25	kn
508	3340.73	3341.6	280.54	707.17	30.83	30.33	<1.31	...	57	0.97	kn
57	3340.74	3307.9	275.84	2054.70	30.90	30.18	0.45	...	78	0.95	kn
59	3340.74	3308.3	277.69	2037.43	30.85	30.21	<1.01	...	81	0.95	kn
170	3340.75	3316.8	274.55	1699.60	30.70	30.39	<0.43	...	108	0.25	kn
76	3340.76	3309.2	270.69	2004.14	29.90	29.56	1.21	...	116	0.08	kn
502	3340.76	3341.8	272.46	697.71	30.70	29.63	<0.92	...	135	0.93	kn
378	3340.78	3333.6	266.18	1027.66	28.64	28.57	0.10	...	129	0.02	kn
636	3340.78	3352.7	266.31	264.62	30.28	29.65	<1.24	...	95	0.95	kn
213	3340.81	3320.3	254.93	1557.44	26.04	26.00	0.29	...	181	0.03	kn
341	3340.81	3331.1	256.46	1127.84	30.47	29.66	<0.91	...	120	0.12	kn
434	3340.82	3337.0	252.96	893.32	29.82	30.07	<0.97	...	69	0.60	kn
523	3340.82	3343.2	253.67	643.19	29.25	28.96	-0.08	...	96	0.03	kn
547	3340.82	3345.5	252.54	549.64	28.84	28.53	<0.43	...	93	0.04	kn
578	3340.82	3349.0	254.82	412.47	24.43	24.44	0.33	...	157	0.03	kn
449	3340.83	3338.3	249.47	839.86	30.73	30.53	0.87	...	57	0.96	kn
386	3340.85	3333.8	245.62	1018.59	29.78	29.43	<0.59	...	93	0.13	kn
603	3340.85	3350.5	244.74	352.09	29.17	28.99	<0.32	...	97	0.01	kn
3	3340.85	3357.3	245.73	80.81	28.43	28.54	0.60	...	89	0.52	aekn
17	3340.86	3304.7	242.73	2184.57	30.17	30.22	0.25	...	48	0.93	ehkn
184	3340.89	3317.7	231.63	1663.71	30.89	29.97	<1.19	...	104	0.85	kn
63	3340.90	3308.6	231.06	2027.66	29.24	29.10	-0.26	...	81	0.19	kn
488	3340.92	3341.1	225.04	728.68	29.32	28.53	<0.76	...	145	0.03	kn
140	3340.93	3315.7	221.71	1744.80	28.56	28.28	0.49	...	105	0.38	bkn
276	3340.93	3325.9	221.88	1335.38	28.20	28.17	0.58	...	85	0.03	kn
579	3340.93	3348.7	221.51	425.17	29.85	29.48	<1.30	...	86	0.71	ekn
139	3340.95	3315.2	213.77	1763.64	27.66	27.59	0.50	...	83	0.37	abkn
72	3340.96	3309.9	213.51	1973.75	31.34	30.29	<0.90	...	86	0.90	kn
257	3340.96	3324.7	213.21	1381.46	30.14	29.97	0.43	...	124	0.05	kn
527	3340.97	3343.5	209.78	631.76	29.23	28.99	<1.04	...	102	0.73	kn
522	3340.99	3343.1	202.09	647.88	30.98	30.21	<1.79	...	77	0.97	kn
83	3341.03	3310.6	192.42	1949.03	31.29	31.23	<1.52	...	44	0.91	kn
387	3341.06	3333.9	183.88	1016.69	28.84	28.57	-0.04	...	90	0.37	kn
443	3341.11	3337.8	166.67	857.97	29.91	30.09	<1.27	...	51	0.82	ehkn
15	3341.12	3304.6	165.61	2189.27	28.51	28.47	0.26	...	71	0.07	ehkn
74	3341.15	3310.5	155.14	1952.26	27.47	27.33	0.29	...	236	0.03	bkn
113	3341.15	3313.0	156.15	1852.35	30.69	30.20	<1.14	...	79	0.97	kn
322	3341.19	3329.6	143.12	1188.50	29.29	29.04	0.57	...	84	0.02	bekn
73	3341.21	3310.1	138.29	1968.22	28.72	28.28	0.30	...	126	0.02	abkn
294	3341.21	3327.8	138.20	1259.52	26.60	26.58	0.61	...	91	0.03	ekn
321	3341.21	3329.8	137.71	1180.86	30.44	30.25	<1.04	...	65	0.97	abekn
112	3341.23	3313.0	133.45	1853.01	29.61	28.98	<0.51	...	91	0.91	kn
156	3341.24	3316.4	130.68	1715.22	29.11	28.23	<0.45	...	233	0.01	kn
311	3341.26	3328.7	122.92	1223.94	30.59	30.42	<1.30	...	38	0.94	ehkn
285	3341.30	3327.0	110.67	1291.43	28.25	28.21	0.62	...	93	0.02	ehkn
280	3341.33	3326.6	103.41	1306.47	28.47	28.47	0.65	...	80	0.06	aehkn
240	3341.35	3322.0	95.88	1492.90	29.70	29.64	<0.30	...	63	0.72	ehkn
87	3341.43	3311.1	73.39	1928.09	30.81	30.07	<0.80	...	78	0.97	dekn
190	3341.44	3318.0	70.10	1650.50	30.56	30.43	<0.67	...	49	0.96	dehkn
109	3341.52	3313.0	46.50	1852.47	25.99	25.73	0.22	...	278	0.03	adehkn

Table 2—Continued

NOTE — Flags: a: Object has near neighbors (50CCD). b: Object was originally blended with another (50CCD). c: At least one pixel is saturated (50CCD). d: Object's aperture data is incomplete or corrupted (50CCD). e: Object is off the image, or within 30 pixels of the edge (50CCD). f: Object lies on top of a diffraction spike (50CCD). g: Photometry is from the second run of SExtractor (50CCD). h: Object is off the image, or within 30 pixels of the edge (F28X50LP). i: Object lies on top of a diffraction spike (F28X50LP). j: Photometry is from the second run of SExtractor (F28X50LP). k: Object is completely off the image (NUV). l: Object is partially off the image (NUV). m: Used global sky value (NUV). n: Object is completely off the image (FUV). o: Object is partially off the image (FUV). p: Used global sky value (FUV). q: Target QSO J2233-606.

Table 3. Source Counts

AB mag	$N_{auto}$	$\log(N_{auto})$	$N_{iso}$	$\log(N_{iso})$
22.75	3	4.46	1	3.99
23.25	2	4.29	2	4.29
23.75	2	4.29	3	4.46
24.25	5	4.68	1	3.99
24.75	7	4.83	5	4.68
25.25	9	4.94	12	5.07
25.75	13	5.10	8	4.89
26.25	19	5.26	15	5.16
26.75	16	5.19	18	5.24
27.25	19	5.26	17	5.22
27.75	28	5.43	17	5.22
28.25	36	5.54	23	5.35
28.75	62	5.78	42	5.61
29.25	74	5.86	55	5.73
29.75	111	6.03	56	5.73
30.25	102	5.99	92	5.95
30.75	72	5.84	82	5.90
31.25	27	5.42	92	5.95
31.75	1	3.99	63	5.79
32.25	1	3.99	8	4.89

Note. — The 50CCD source counts. Magnitudes are in the AB magnitude system. The counts are given for the SExtractor MAG\_AUTO, which uses an elliptical aperture set at 2.5 times the first moment of the semi-major and semi-minor axes. We also give the counts as determined using isophotal magnitudes. Column 1 is the center of the magnitude bin, columns 2 & 4 contain the raw number of objects per bin in the image, and columns 3 & 5 contain the log of the number per magnitude per square degree.